DEVELOPMENT AND IMPLEMENTATION OF ULTRAFAST ULTRASOUND IMAGING

A THESIS SUBMITTED TO
THE GRADUATE SCHOOL OF NATURAL AND APPLIED SCIENCES
OF
MIDDLE EAST TECHNICAL UNIVERSITY

BY

EDA BEGÜM BERBEROĞLU

IN PARTIAL FULFILLMENT OF THE REQUIREMENTS
FOR
THE DEGREE OF MASTER OF SCIENCE
IN
ELECTRICAL AND ELECTRONICS ENGINEERING

JANUARY 2022

Approval of the thesis:

DEVELOPMENT AND IMPLEMENTATION OF ULTRAFAST ULTRASOUND IMAGING

submitted by **EDA BEGÜM BERBEROĞLU** in partial fulfillment of the requirements for the degree of **Master of Science** in **Electrical and Electronics Engineering, Middle East Technical University** by,

Prof. Dr. Halil Kalıpçılar
Dean, Graduate School of **Natural and Applied Sciences** _____

Prof. Dr. İlkay Ulusoy
Head of the Department, **Electrical and Electronics Engineering** _____

Prof. Dr. Barış Bayram
Supervisor, **Electrical and Electronics Engineering, METU** _____

Examining Committee Members:

Prof. Dr. Abdullah Atalar
Electrical and Electronics Engineering, Bilkent University _____

Prof. Dr. Barış Bayram
Electrical and Electronics Engineering, METU _____

Prof. Dr. Çağatay Candan
Electrical and Electronics Engineering, METU _____

Assoc. Prof. Dr. Serdar Kocaman
Electrical and Electronics Engineering, METU _____

Assoc. Prof. Dr. Selçuk Yerci
Electrical and Electronics Engineering, METU _____

Date: 25.01.2022

I hereby declare that all information in this document has been obtained and presented in accordance with academic rules and ethical conduct. I also declare that, as required by these rules and conduct, I have fully cited and referenced all material and results that are not original to this work.

Name Last name : Eda Begüm Berberoğlu

Signature :

ABSTRACT

DEVELOPMENT AND IMPLEMENTATION OF ULTRAFAST ULTRASOUND IMAGING

Berberoğlu, Eda Begüm
Master of Science, Electrical and Electronics Engineering
Supervisor : Prof. Dr. Barış Bayram

January 2022, 75 pages

Ultrasound imaging provides noninvasive, safe and real-time visualization for soft tissues. Ultrasound contrast agents have been used to improve imaging performance by enhancing echo signals for diagnostic and therapeutic purposes. Plane wave imaging started a new era on ultrasound imaging due to providing high frame rate acquisitions, which enabled ultrasound imaging well below the diffraction limit. In this thesis, super resolution ultrasound imaging technique was investigated by localizing individual microbubbles (MBs) in a capillary tube. The programmable Verasonics Research System with a 128-element linear transducer array was used to conduct experiments. Different sequences were developed and their performance were evaluated in imaging experiments of coherent compounding plane wave imaging (CPCW) and pulse inversion (PI) with compounding angles. For removing tissue signals and detecting MBs; differential imaging (DI), PI and singular value decomposition (SVD) filtering techniques were implemented successfully. Ultrasound imaging system was characterized in terms of lateral and axial resolution by extracting point spread function (PSF) for different imaging modalities. Furthermore, acoustic radiation force (ARF) was combined with ultrafast ultrasound imaging in order to direct MBs towards the bottom wall of the capillary tube. Effect of using different transmit voltages, flow rates and number of angles was evaluated

in terms of via image quality metrics such as contrast to tissue ratio (CTR), contrast to noise ratio (CNR).

Keywords: Ultrasound imaging, super resolution ultrasound, microbubble, high frame rate imaging, transducer.

ÖZ

YÜKSEK HIZLI ULTRASON GÖRÜNTÜLEMENİN GELİŞTİRİLMESİ VE UYGULANMASI

Berberoğlu, Eda Begüm
Yüksek Lisans, Elektrik ve Elektronik Mühendisliği
Tez Yöneticisi: Prof. Dr. Barış Bayram

Ocak 2022, 75 sayfa

Ultrason görüntüleme, yumuşak dokuların müdahale gerektirmeyen, güvenli ve anlık canlı bir şekilde görüntülenmesini sağlar. Ultrason kontrast maddeleri, teşhis ve tedavi amaçları için yankı sinyallerini güçlendirerek görüntüleme performansını iyileştirmek için kullanılmıştır. Düzlem dalga görüntüleme, kırınım sınırının çok altında ultrason görüntülemeyi mümkün kılan yüksek kare hızlı kazanımlar sağlaması nedeniyle ultrason görüntülemede yeni bir dönem başlattı. Bu tezde, tüpün içerisinde mikrobaloncuklar (MBler) tekil bir şekilde lokalize edilerek yüksek çözünürlüklü ultrason görüntüleme tekniği araştırılmıştır. Deneyleri gerçekleştirmek için programlanabilir Verasonics Araştırma Sistemi ve 128 elemanlı lineer çevirgeç kullanmıştır. Bağdaşık bileştirmeli düzlemsel dalga ile görüntüleme, dalga evirme ile görüntüleme gibi farklı birtakım görüntüleme kodları tasarlanmıştır. Dokudan gelen sinyalleri temizlemek ve mikrobaloncukları tespit edebilmek amacıyla görüntüler arası fark alma algoritması ve tekil değer ayrıştırma filtresi uygulanmıştır. Ultrason görüntüleme sistemi, farklı görüntüleme modaliteleri için nokta yayılma fonksiyonu (PSF) çıkarılarak yanal ve eksenel çözünürlük açısından karakterize edildi. Ayrıca, akustik radyasyon kuvveti (ARF), MB'leri kılcal borunun alt duvarına yönlendirmek için ultra hızlı ultrason görüntüleme ile birleştirildi. Farklı voltaj

değerleri, akış hızları ve açı sayısının kullanılması sonucu elde edilen veriler tespit edilen mikrobaloncuk sayısı ve birtakım nitelik ölçütleri olan kontrast-doku oranı (CTR), kontrast-gürültü oranı (CNR) doğrultusunda incelenmiştir.

Anahtar Kelimeler: Ultrason görüntüleme, yüksek çözünürlüklü ultrason, mikrobaloncuk, yüksek hızlı görüntüleme, çevirgeç.

To My Beloved Family

ACKNOWLEDGEMENTS

This thesis is funded by Scientific and Technological Research Council of Turkey (TÜBİTAK) under grant number 116E642.

During the procession of this study, the author acknowledges the financial support of TUBITAK BIDEB 2210-A 2018-1 Scholarship.

The author wishes to express her deepest gratitude to her supervisor Prof. Dr. Barış for his enlightening guidance, insight and support throughout the research.

I would like to thank, Prof. Dr. Abdullah Atalar, Prof. Dr. Çağatay Candan, Assoc. Prof. Dr. Serdar Kocaman and Assoc. Prof. Dr. Selçuk Yerci, for being on my thesis committee.

I would like to thank Prof. Dr. Asaf Behzat Şahin and Assoc. Prof. Dr. Ömer Karal for their technical support.

The technical assistance of Prof. Dr. Hüseyin Avni Öktem, Dr. Yiğit Aksoy, and Mrs. Zeynep Öktem under Nanobiz Technology are gratefully acknowledged.

I would like to thank Ms. Zeynep Ece Kızılateş for her technical support during ultrasound imaging experiments.

I would like to thank the members of ULTRAMEMS Research Group, Mr. Berkay Karacaer, Ms. Berre Vize and Mr. Cemil Cömert for their technical support and useful discussions.

Finally, I want to express my deep appreciation to my family for their endless support.

TABLE OF CONTENTS

LIST OF TABLES

TABLES

LIST OF FIGURES

FIGURES

CHAPTER 1

INTRODUCTION

Medical ultrasound (1 – 50 MHz) has applications in imaging (e.g. fetal sonogram), therapeutics (e.g. kidney stone ablation), and detection (e.g. brain haemorrhage). Today, medical ultrasound is not only a standalone technology worth of > $7B but also an integral part of other emerging (e.g. photoacoustic) medical applications using ultrasound techniques such as continuous or pulsed wave Doppler (colour, power and spectral) [1], shear wave elastography (point, 1D and 2D) [2, 3], contrast enhanced ultrafast and super resolution ultrasound (microbubbles for blood and neurovascular imaging) [4-7]. Medical ultrasound is expected to grow 23% annually in the next five years. Diagnostic imaging used for detection of anomaly in lungs [8], characterization of hand tendons [9], determination of Down Syndrome [10], visualization of fibrosis in pancreatic ductal adenocarcinoma [11], functional neuroimaging [12], therapy used for blood-brain barrier opening procedures [13] and cancer treatment [14] are only a few of the advanced medical ultrasound applications to present the immense potential of ultrasound for public health and well-being.

Ultrasound is a superior imaging technique among many modalities (X-ray, computed tomography (CT), magnetic resonance (MR), etc.) which is preferable due to its good soft-tissue contrast, portability, non-damaging, and cost-effective features. Real-time image presentation of the ultrasound imaging technology enables the study of moving internal structures [15]. The commonly used application areas of ultrasound imaging in medicine are imaging of cardiac structures, the vascular system, the fetus and uterus, abdominal organs such as the liver, kidneys and gall bladder, and the eye.

Another application of ultrasound in the medical community is for therapeutic use. The capability of generating a precise ablation pattern deep in tissue without any effect on surrounding structures is the noticeable benefit of using high intensity focused ultrasound (HIFU) over other modalities used in therapeutic applications, e.g., radio-frequency (RF) ablation [15]. Nowadays, focused ultrasound has exciting potential for treating prostate, breast, and liver cancer.

This thesis is focused on contrast enhanced ultrasound imaging application which uses ultrasound contrast agents to image an area by increasing signal to noise ratio for diagnostic use. Mainly, cancer-causing molecules are found within the blood circulating in vessels, especially in tiny capillaries. Before accumulating in large amounts in the tissues, these trace amount of cancer-causing molecules will adhere to the wall of the capillaries. Targeting ligands can be attached to preformed microbubbles. This is often achieved by use of the strong noncovalent interaction between streptavidin or biotin, which are generally bound to the microbubble surface and to a specific antibody.

In this thesis, an application for detection of these molecules via ultrasound blood vessel imaging using MBs is presented. Imaging algorithms related to this study were developed and tested in the laboratory using ultrasound imaging hardware (Verasonics Inc., WA, USA). For intravascular blood flow mimicking, a plastic capillary tube and a microbubble mixture with phosphate buffered saline in a syringe pump was provided with a controlled adjustable flow rate. While ultrafast method was used collecting thousands of images per second, the use of focused ultrasound (FUS) simultaneously moved the MBs in the direction perpendicular to their formation rate with the force of acoustic radiation, and contact of the MBs with the tube wall was shown. The binding of streptavidin-coated MBs with antibody-antigen interaction customizable quality with the antibody in the tube wall can be detected by simultaneous ultrafast ultrasound imaging. This thesis study, based on the interaction of MB-antibody with FUS in the laboratory environment, is a pioneer in the development of unique devices in the field of health.

Cancer causing molecules are freely circulating in blood vessels, especially in capillaries, and stick to the capillary wall in some regions long before causing palpable discomfort at the organ or tissue level. An application for the detection of such molecules via an affordable method such as ultrasound imaging will be of utmost importance to create added value for public health and well-being of the society. Acoustic radiation force (ARF) steers microbubbles, and ultrafast ultrasound imaging can simultaneously detect accumulation of streptavidin-coated microbubbles due to its reaction with the antibody placed within the capillary tube walls.

The milestones of this project concerning ultrasound imaging can be grouped into five steps. Firstly, an experimental setup is designed and physically constructed. This step includes understanding microbubble dynamics, selecting proper contrast agent for our experimental setup and preparing microbubble suspension with appropriate dosage. The second step is the algorithm development for implementing different ultrasound imaging techniques on our imaging system such as plane wave imaging with compounding angles, harmonic imaging etc. The third milestone is the development and implementation of preprocessing methods. These methods are used to eliminate tissue signals and highlight microbubble signals by filtering out background and noise using methods such as differential imaging, pulse inversion and singular value decomposition (SVD) filtering. After that, post-processing algorithms are developed to detect individual microbubbles which are smaller than diffraction limit of ultrasound imaging. Therefore, ultrasound localization microscopy (ULM) steps such as generation of point spread function (PSF), two-dimensional cross correlation (2D-CC) with PSF, nonlocal means (NLM) filtering are applied. Therefore, tracking of localized microbubbles is performed using Hungarian tracking algorithm to follow individual microbubble location in each frame. The velocity map of MBs is extracted to determine the effectiveness of proposed ultrafast ultrasound imaging with acoustic radiation force (ARF) method in terms of the manipulation of MBs via ARF.

The Contribution of the thesis

- An ultrafast imaging algorithm was designed and implemented for the imaging of MBs in a capillary tube.
- ARF was implemented in combination with the ultrafast imaging for simultaneous adjustment of MBs position and imaging in a capillary tube.
- The imaging quality was enhanced by the implementation of state-of-the-art imaging techniques such as differential imaging (DI), pulse inversion (PI) and singular value decomposition (SVD).
- Streptavidin coated MBs were pushed ultrasonically towards the bottom glass wall of the capillary tube via intertwined ARF and imaging pulses.

This thesis presents a new highly effective method for simultaneous manipulation and imaging of MBs, and this method, employed in a health-related feasible implementation, can be used for early detection of cancer molecules in-vivo via imaging blood.

CHAPTER 2

ULTRASOUND IMAGING TECHNIQUES

Ultrasound imaging techniques are overviewed including the recent development of the area that enables high frame rate imaging and contrast enhanced ultrasound (CEUS) imaging techniques. Then, different CEUS techniques are explained in detail.

2.1 Conventional Ultrasound Imaging

Conventional ultrasound imaging transmits line-per-line focused beams from each element of the transducer sequentially and receive from all elements to form one image line. This process repeats until all image lines are collected and ready to form one image, illustrated in Figure 2.1.

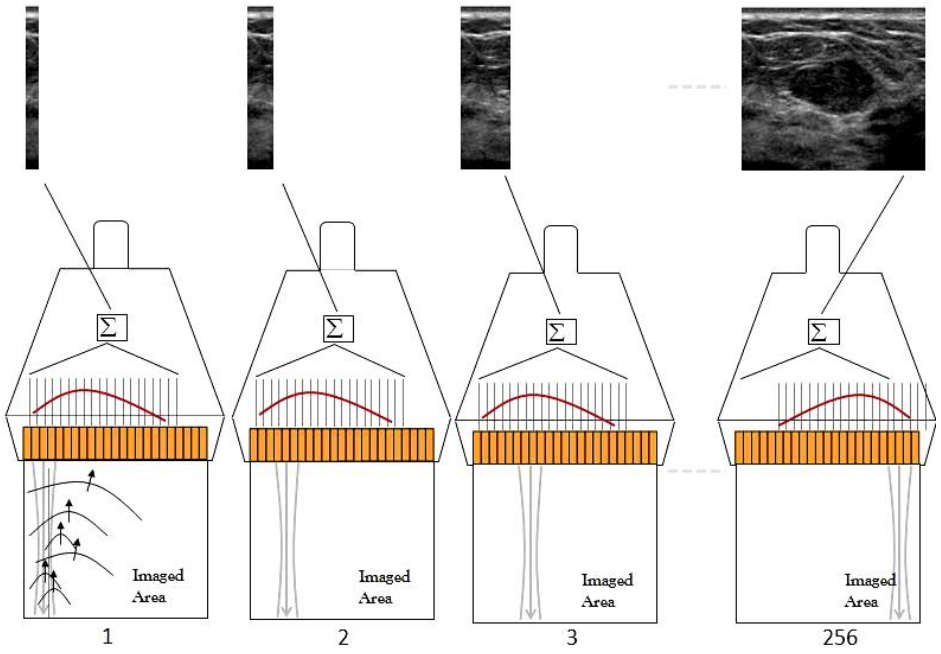

Figure 2.1. Conventional Ultrasound Imaging Topologies [16].

Total time to form one image and hence frame rate of the imaging sequence can be calculated by equations (2.1) and (2.2), where N_{lines} represents number of lines in the image, Z represents image depth, and c is the speed of ultrasound wave (1540 m/s).

$$T_{image} = \frac{N_{lines} * 2 * Z}{c} \quad (2.1)$$

$$FR_{max} = \frac{1}{T_{image}} = \sim 24\text{-}60 \text{ fps} \quad (2.2)$$

There have been many innovations that took place in the ultrasound imaging field such as parallel processing of many channels at the same time with graphics processing units (GPUs) and fast data bus links (PCI express technology) capable of transferring huge amount of data to these units. These recent improvements provide the transition from conventional ultrasound to ultrafast ultrasound imaging.

2.2 Ultrafast Ultrasound Imaging

Ultrafast ultrasound imaging utilizes plane waves or divergent waves instead of focused beams to achieve high frame rates. Plane waves are generated applying proper delay on the elements of the transducer. The main idea is obtaining entire image with a single transmission covering whole area. Therefore, plane wave imaging has high temporal resolution (>= 1000 fps) in expense of lower spatial resolution and contrast of the images. Ultrafast ultrasound imaging allows capturing fast moving objects like microbubbles.

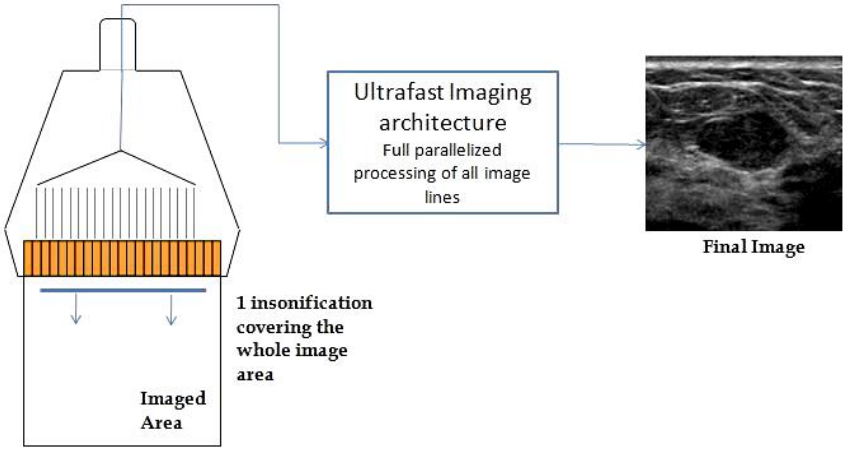

Figure 2.2. Ultrafast ultrasound imaging topology [16].

Lack of focusing during plane wave imaging causes the reduction in image quality [17]. To improve image quality, coherent plane wave compounding (CPCW) method is proposed as shown in Figure 2.3. Ultrafast imaging is applied with seven steering angles ranging between ± 10°. Increasing number of steering improves image quality while reducing the frame rate as shown in Figure 2.4. Chosen angle range ensures that the target is located within the overlapped region of all plane waves. The beamformed data from all angles are summed coherently to obtain a high-quality image. Plane wave imaging spreads out the spatial peak acoustic intensities over more pulses allowing for imaging at lower mechanical index (MI). Since the peak pressure is decreased, unwanted destruction of microbubbles is less likely to occur [18].

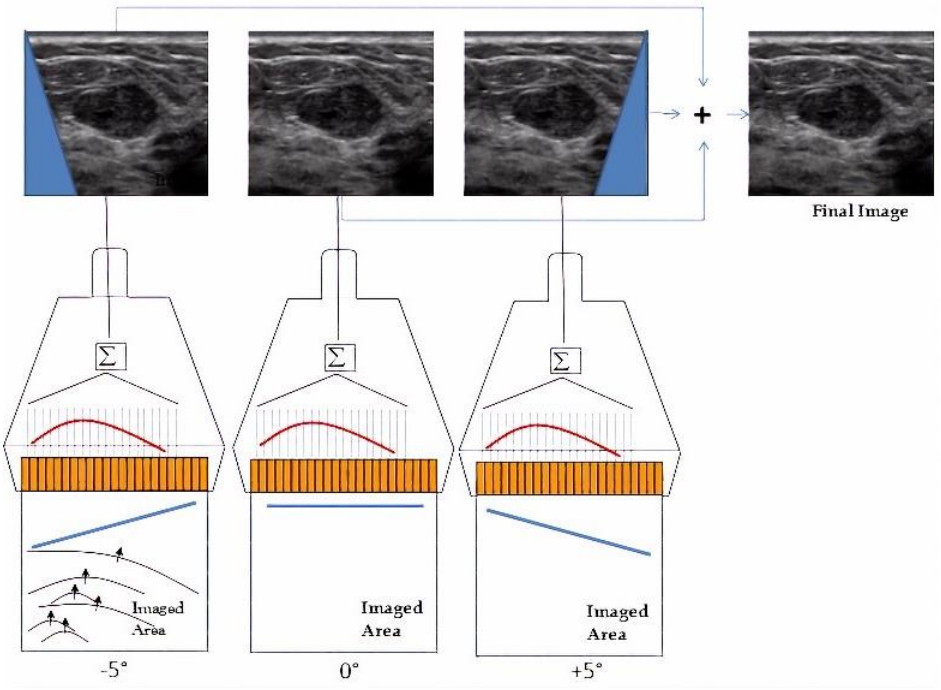

Figure 2.3. Coherent plane wave compounding imaging topology [16].

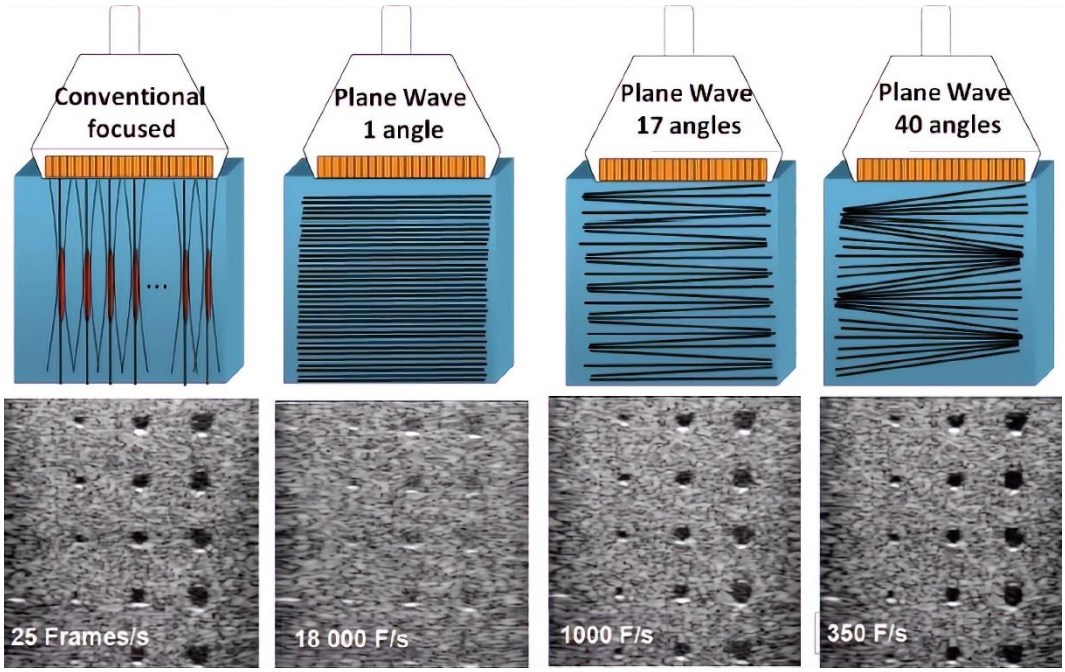

Figure 2.4. Conventional focused and plane-waves with/without compounding angles imaging illustration with corresponding frame rates [4].

2.3 Super-Resolution Ultrasound Imaging

Conventional imaging methods are based on waves and therefore the resolution of ultrasound imaging is limited by λ /2. Diffraction is a physical phenomenon of wave bending while passing through an opening in the order of the wavelength. Diffraction also occurs when an ultrasound wave travels through a medium with a varying acoustic impedance. Diffraction is the determining factor for spatial resolution because it causes two point-sources which are close to each other to blur and to be detected as a single source. Two objects standing closer than the half of the wavelength of the transmit frequency cannot be resolved due to the finite size of the elements [19].

Resolution limit of λ/20 can be achieved with super resolution ultrasound techniques (SRUS) [20]. The diffraction-limit can be overcome by super-localizing single events from isolated sources. Ultrafast processes such as rapid movement of ultrasound contrast agents (UCAs) can be monitored beyond the diffraction limit.

Ultrasound Localization Microscopy (ULM) Ultrasound localization microscopy refers to a super-resolution ultrasound technique. In this technique, super-resolved final image is composed of localization of individual microbubbles obtained from huge number of frames in time. For proper localization in ULM, localization sources should be sparce in space [21-23].

2.4 Contrast Enhanced Ultrasound Imaging Techniques

Contrast enhanced ultrasound imaging is conducted with the introduction of contrast agents. Ultrasound contrast agents (UCAs) are developed to obtain greater backscattering signals so that contrast of images can be improved and tissues that cannot be observed normally become visible. A microbubble scatter echoes 140 dB more than a single blood cell. However, total number of MBs will be much less than the total number of blood cells in clinical applications and hence the actual increase in echogenity is around 20 dB [24]. Contrast agents are clinically used to see the difference between normal and diseased tissues, to get better-quality images of an abnormality, to monitor blood flow and to check the existence of clots in a vessel. In addition, contrast agents can be produced in a way that they target specific substance to transfer drugs and defuse diseased cells. The most common contrast agents are microbubbles (MBs) and nanodroplets. More information about MBs are provided in the following chapter (Chapter 3.1). Some CEUS imaging techniques are summarized in the following part of this chapter.

2.4.1 Differential Imaging Method

Differential imaging (DI) method can be applied with 1) the subtraction of raw RF data (before beamforming process) of adjacent (frame-to-frame) frames and the subtraction of adjacent images or subtraction of the base background image from the all acquired images. Moving or disrupted objects between frames, i.e., blinking MBs, generates the difference signal while stationary tissue signals and constant microbubble signals are removed [25].

Differential imaging method is used for eliminating background signal and increasing contrast in final images to detect MBs. DI technique gives effective results in ex-vivo experiments where there is no tissue movement. Otherwise, DI can be used by applying motion correction algorithm (i.e., “imregcorr.m” function in Matlab) first to remove tissue motion [26]. However, DI method is only appropriate for fast blood flows (>0.75 mm/s) and useful for axial flows more than lateral component of the movement [27].

DI method is simple and computationally inexpensive method compared to PI and SVD methods. Therefore, DI might be a preferable method when the suitable conditions are met such as fast and axial blood flow during high frame rate imaging.

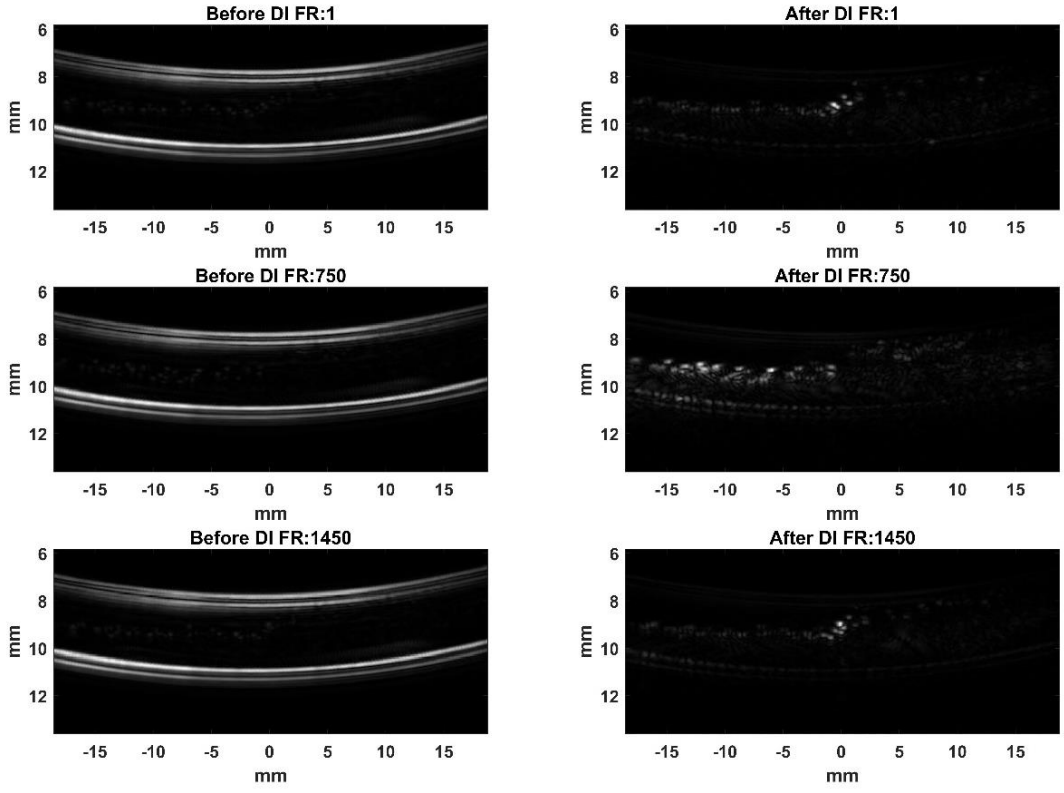

Figure 2.5. Frame to frame subtraction of experimental data.

2.4.2 Pulse Inversion Method

Pulse inversion (PI) is a method that isolates nonlinear signals from linear background signals. In this method, temporally adjacent two transmit pulses whose polarities are opposite are transmitted and RF data of received signals are summed before beamforming. As shown in Figure 2.6, linear components of echo signals are canceled after summation since the linear component of the received echoes are the same except their polarities. On the other hand, nonlinear components of echo signals are remained intact and are highlighted after summation due to the random behavior of the nonlinear components.

The harmonics produced by MBs allow PI technique to isolate MBs from background. Although filters can be used to extract harmonics without applying any imaging technique, PI shows superiority in terms of reducing interference of harmonics with linear components and preventing contrast reduction due to spectral leakage. Nonlinearity coming from transducer itself causes spectral leakage that cannot be filtered out. The most obvious disadvantage of PI is lowering temporal resolution to a minimum of two times because two transmissions are needed for each data [27, 28].

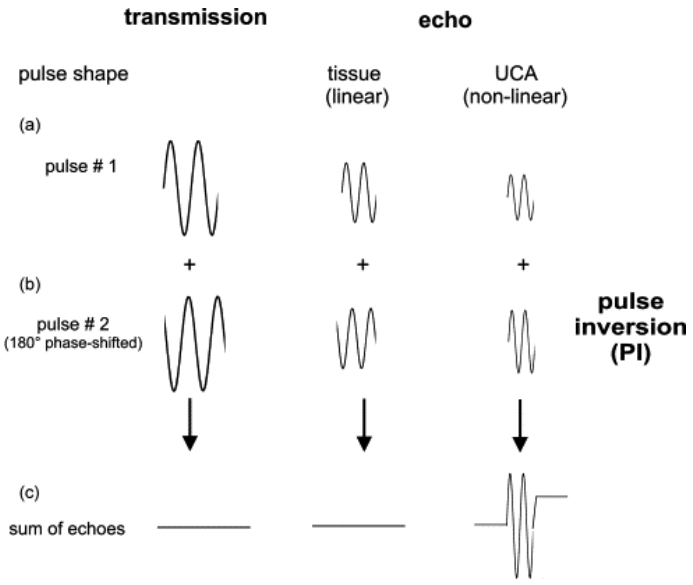

Figure 2.6. Pulse inversion method. (a) Positive transmit signal, (b) Negative transmit signal (c) Summation of echoes results in amplified nonlinear echo [29].

PI technique can be defined mathematically as follows:

$$y_{-}(t) = a_1.x(t) + a_2.x(t)^2 + a_3.x(t)^3 + \cdots \quad (2.3)$$

$$y_{+}(t) = -a_1.x(t) + a_2.x(t)^2 - a_3.x(t)^3 + \cdots \quad (2.4)$$

$$y_{sum}(t) = y_{-}(t) + y_{+}(t) = 2a_2.x(t)^2 + 2a_4.x(t)^4 + \cdots \quad (2.5)$$

where $x(t)$ is the transmit pulse and $y_{sum}(t)$ is the summed echo signal. As can be calculated from equations (2.3) and (2.4), PI technique enhances second harmonics of the transmit signal. In addition, the signal amplitude is increased with a factor of 2 whereas noise decreases with a factor of $\sqrt{2}$. Thus, a SNR is increased by $\sqrt{2}$ with PI technique.

At low pressures (<100 kPa), second harmonics may be used for contrast specific applications. However, at normal imaging pressure (<1 MPa), the second harmonic enhancements were minimal. Second harmonic is produced not only by contrast agents but also nonlinear propagation of ultrasound in water or tissue. Therefore, second harmonic enhancements are not unique to contrast agents [30]. Second harmonic emission from tissue is generated due to wave propagation through tissue and is not produced due to reflection. MBs form harmonics due to their expansion and contraction under ultrasound wave which is an exceptional statement. Nonlinearity coming from tissue distorts the sine wave during its propagation through tissue because the propagation speed is higher in compressed regions of tissue compared to expanded regions. This distortion will result in the generation of harmonic frequencies from tissue. The harmonic generation highly depends on the mechanical index, pulse length and the total distance travelled by ultrasound wave. Harmonics produced by tissue increase with increasing mechanical index [31-32]. Tissue originated harmonics are produced when MI> 0.3. However, when MI>0.1, microbubbles are destructed. Therefore, second harmonic enhancements should have belonged to MBs during real-time imaging of MBs [33]. It should be noted that second harmonic enhancements decrease with increasing pressure.

2.4.3 Harmonic Imaging Method

Microbubbles generate second order harmonics of transmit signal frequency. In addition to second and higher order harmonics (2f, 3f,…), nonlinear oscillation of MBs leads to generation of subharmonic (f/2, f/3, …) and ultraharmonic (3f/2, 5f/2, …) components in echo signal [30]. The fundamental and the harmonic frequencies generated by MBs are shown in Figure 2.7.

Subharmonic and ultraharmonic enhancements are unique to MBs and they show stronger echo signal with the increasing transmit pressure so that they can be as effective as second harmonics. In addition, ultraharmonic imaging yields in better image resolution due to its higher frequency compared to subharmonic imaging [30, 33].

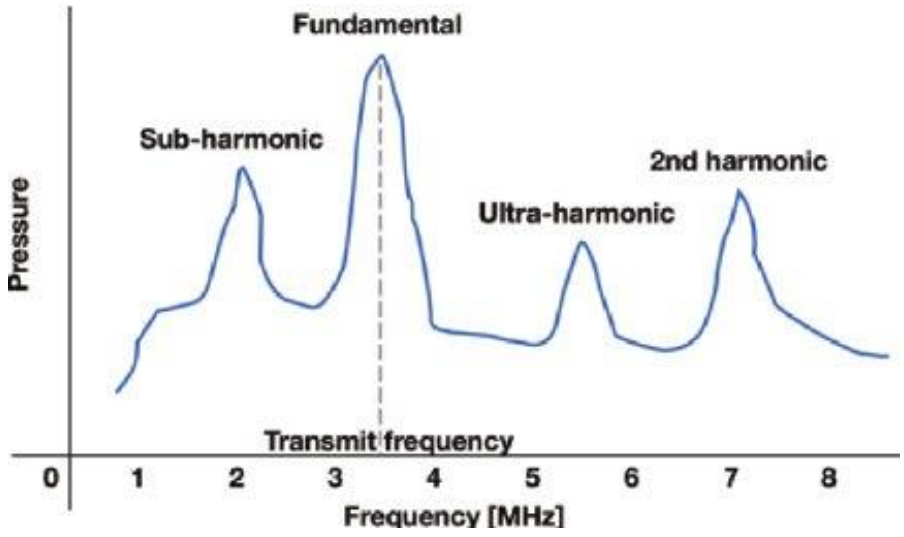

Figure 2.7. Fundamental, second harmonic, subharmonic, and ultraharmonic frequencies of the MB [31].

Response of nonlinear systems to a sinusoidal input will generate frequencies that are multiples of transmit frequency. However, output of nonlinear systems may contain half of the driven frequency (subharmonic) components under proper conditions such as acoustic pressure exceeding a certain threshold value. Generation of subharmonic response from microbubbles has been investigated for more than five decades. The mathematical approach about the source of subharmonic

generations was presented in one of the pioneer studies on emission of subharmonics [34]. Firstly, motion equation for a microbubble under pressure in a liquid has been described and solved. Then, the periodic solution for motion equation is found to be unstable for certain values of pressure and frequency and one of this unstable frequency values corresponds to subharmonic.

In addition, the hysteresis behavior of the microbubble radius depending on frequency change was calculated as a physical mechanism of subharmonic emission. Microbubbles show asymmetrical behavior due to increasing and decreasing frequency. While microbubbles expand, there is an unlimited range of expansion with the decrease in surface tension of the MB due to spring softening effect during expansion. On the other hand, while the microbubbles shrink, there is a limited range of shrinkage due to the increase in gas pressure due to spring hardening effect during compression [35].

In more recent works [36], it is presented that the change in the elasticity of the bubble shell as a function of bubble radius enhances the subharmonic behavior of the microbubbles. Instead of using a purely linear viscoelastic model, if the shell elasticity of the phospholipid shell is assumed to vary with the bubble radius, the rapid change in the elasticity of the bubble shell (as proposed in the model of Marmottant) is found to be responsible for the enhancement of the subharmonic behavior of microbubbles.

Furthermore, gas inside the microbubble expands and shrinks continuously under the negative and positive pressure, respectively. Heat energy generated during this process causes temperature to increase in gas and hence the heated gas may cause the delayed microbubble expansion reaction. The subharmonic emission depends on the type of core gas, mainly polytropic index, and appears to be consistent with the experimental observation of the increasing subharmonic response of the microbubble with heating under compressed state [37].

The main disadvantage of harmonic imaging is the dependency on the bandwidth of the transducer. Bandwidth of the 128-elements linear transducer array, L11-5v

(Verasonics Inc., WA, USA), is presented in Figure 2.8. For harmonic imaging experiments, the most appropriate transmit frequency range is 5-6 MHz to make sure that subharmonic, ultraharmonic and second harmonic regions are covered by the bandwidth of the transducer.

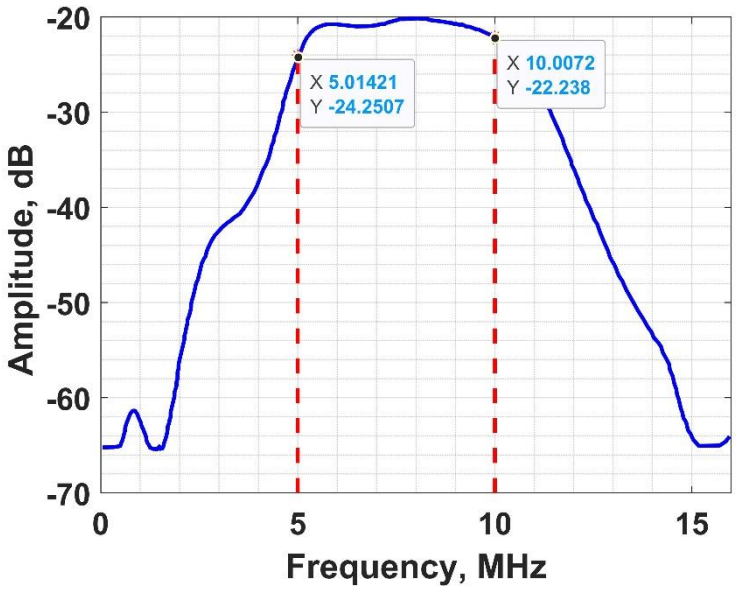

Figure 2.8. Spectrum of L11-5V transducer.

Implementation of subharmonic and ultraharmonic imaging requires filtering of receive signals at fundamental frequency. Therefore, only responses from harmonic frequencies are collected as received RF data. FIR filters for receive process is designed by using "FilterTool" of Verasonics.

- Ultraharmonic Imaging: FIR (finite impulse response) filter is designed to eliminate the responses from fundamental and second harmonic regions. As 1.5 harmonic frequency is in receive bandwidth of the transducer, sensitivity might even improve.

- Subharmonic Imaging: FIR (finite impulse response) filter is designed to eliminate the responses from fundamental frequency and allows receiving signals from $f_0/2$. Tissue does not generate components for subharmonic region so signal detection for this region must definitely originate from microbubbles.

Considering the spectrum of L11-5v transducer, it is very challenging to choose proper fundamental frequency that covers both f0/2 and 3f0/2. It has been decided to use 6.25 MHz as the fundamental frequency, which means subharmonic signals will occur at 3.12 MHz, and ultraharmonic signals will occur at 9.37 MHz. Designed FIR filter for subharmonic region, has 60 dB suppression for fundamental frequency and it means approximately 40 dB difference in echo amplitudes between $f_0/2$ and f_0 frequencies. However, better results are expected for ultraharmonic region since $3f_0/2$ is in receive bandwidth and loss in echo signal is minimal compared to subharmonic region. In Figure 2.12, an example of an image obtained by harmonic imaging at second harmonics region.

For the filter design for second harmonic region, a filter with 3 dB bandwidth 22 % from 10.59 to 13.15 MHz and a stopband of 20 dB points from 9.52 to 14.1 MHz is used as stated in Figure 2.9. For the filter design for ultraharmonic region, filter with 3 dB bandwidth 42 % from 7.42 to 11.32 MHz and a stopband of 20 dB points from 6.38 to 12.39 MHz is used as stated in Figure 2.10. For the filter design for subharmonic region, a filter with 3 dB bandwidth 39 % from 2.50 to 3.72 MHz and a stopband of 20 dB points from 1.62 to 4.64 MHz is used as stated in Figure 2.11.

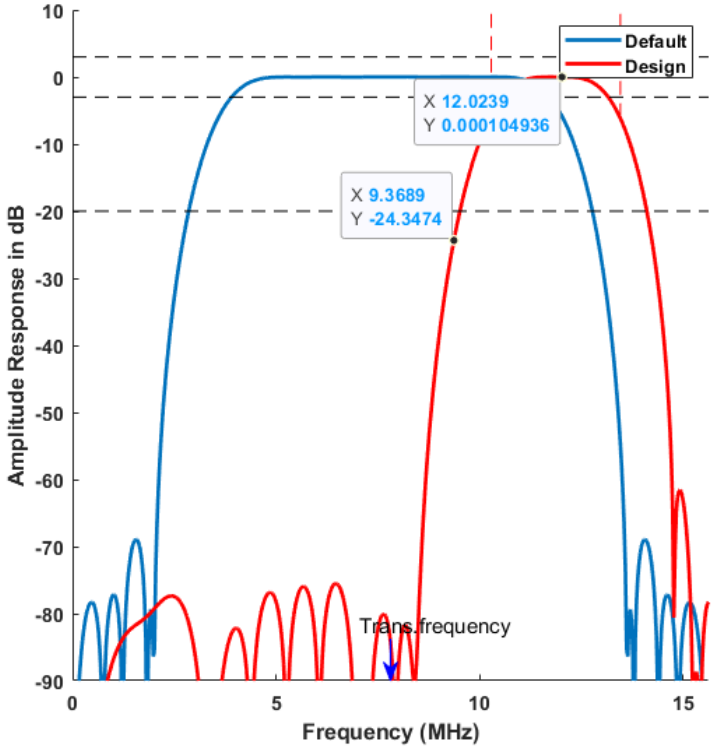

Figure 2.9. FIR filter design for second harmonic region.

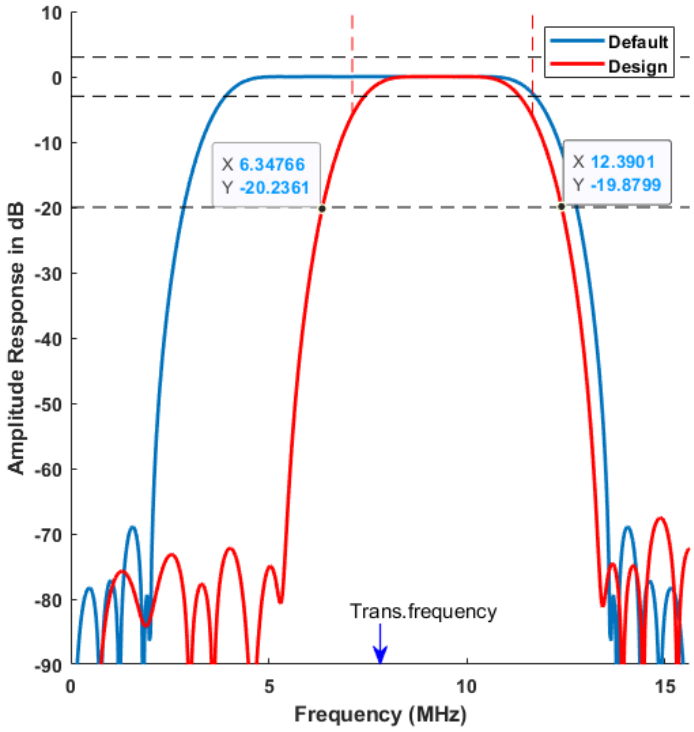

Figure 2.10. FIR filter design for ultraharmonic region.

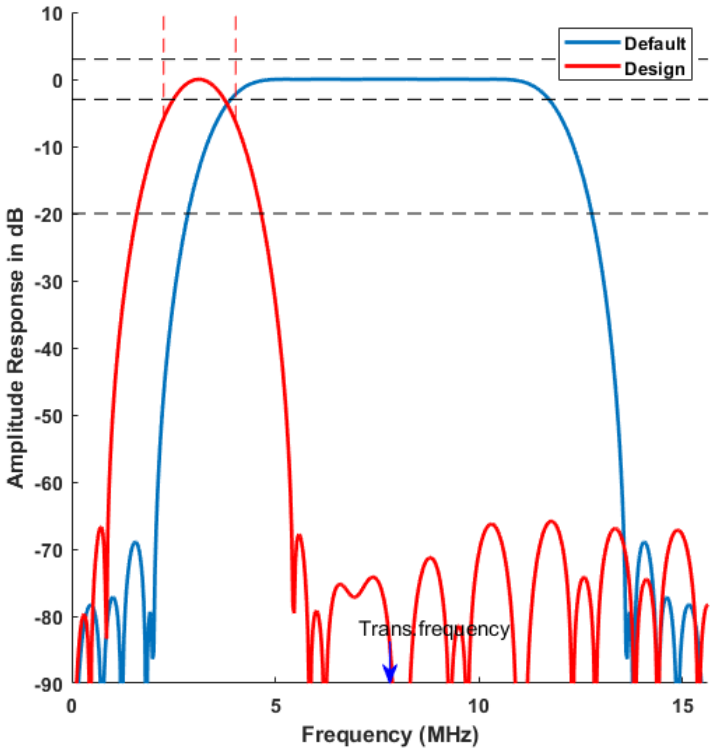

Figure 2.11. FIR filter design for subharmonic region.

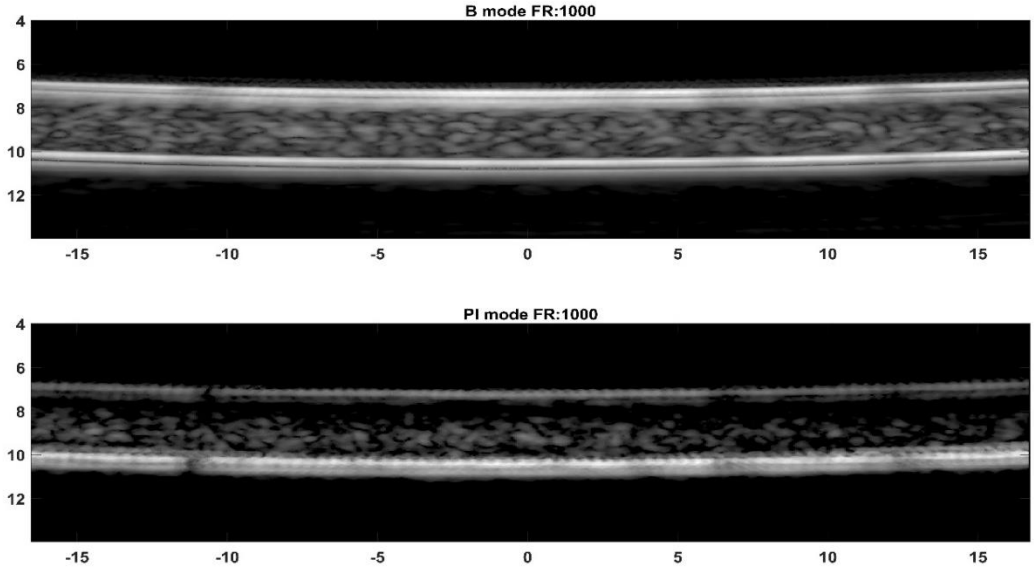

Figure 2.12. B mode image vs PI applied image.

CHAPTER 3

DEVELOPMENT OF ULTRAFAST IMAGING WITH ACOUSTIC RADIATION FORCE

Materials and imaging methods used in the experiments are presented. Firstly, microbubbles, Verasonics Vantage System and experimental setup are overviewed. Then, designed ultrasonic imaging scripts are presented to apply contrast enhanced ultrasound imaging techniques.

3.1 Microbubbles as Ultrasound Contrast Agents

Ultrasound contrast agents are usually used for targeted drug delivery, detection of blood flow and diagnosis regarding any vascular imaging. Technological developments in ultrasound imaging enable ultrasound contrast agents to be an effective tool for improving diagnosis quality thanks to their strong backscattering property, ability to propagate nonlinearly and harmonic generation.

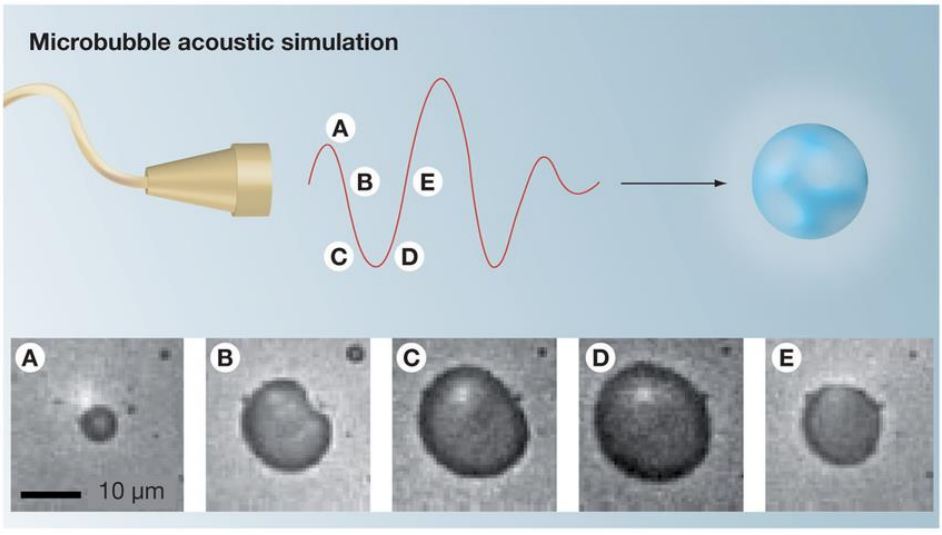

Figure 3.1. Ultrasound interaction with MBs [38].

Physically, microbubbles (MBs) are small gas encapsulated spheres with typically 1-10μm diameter size. MBs are ultrasound sensitive agents meaning that they start to oscillate when ultrasound signal is applied. Microbubbles shrink during the positive cycle of the transmitted signal whereas they expand during the negative cycle of the transmitted signal as indicated in Figure 3.1. The frequency value that oscillation reaches its peak called resonance frequency. Factors such as diameter, shell and core gas materials of microbubble play significant roles in resonance frequency [38]. There are several mathematical models in the literature to understand encapsulating microbubble behavior under ultrasound excitation. Church model equation is derived from Rayleigh-Plesset model (free gas bubble model) but included the effect of shell thickness and viscoelastic properties. The resonance frequency of the encapsulated with lipid shell bubble was approximated by using Equations 3.1, 3.2, and 3.3, and Table 3.1 [39].

$$f_0 = \frac{1}{2\pi a_0 \left[\rho_{s0}\left(1+\Delta_\rho\, {a_0}/{R_0}\right)\right]^{1/2}} \times$$

$$\{3\kappa p_0 - \frac{2\sigma_1}{a_0} - \frac{2\sigma_2 a_0^3}{R_0^4} + \cdots 4G_s\left(1-\frac{a_0^3}{R_0^3}\right)\left[1+\left(1+\frac{3a_0^3}{R_0^3}\right)Z\right]\}^{1/2} \quad (3.1)$$

$$Z = \frac{1}{2G_s}\left(\frac{\sigma_1}{a_0}+\frac{\sigma_2}{R_0}\right) \quad (3.2)$$

$$\Delta_\rho = \frac{\rho_{l0}-\rho_{s0}}{\rho_{s0}} \quad (3.3)$$

Table 3.1. Parameters for resonance frequency calculation of MBs.

Model parameters	Variable	Value	Unit
Density of shell	ρ_{s0}	1100	kg/m^3
Density of exterior media	ρ_{l0}	1000	kg/m^3
Normalized density difference between liquid and shell	Δ_0	-0.091	-
Inner radius of shell	a_0	R_0-d	μm
Outer radius of shell	R_0	variable	μm
Shell thickness	d	3	nm
Polytropic exponent	κ	1.1	-
Initial gas pressure	p_0	101.3	Pa
Surface tension between inner surface of the shell and interior media	σ_1	0.04	Pa.m
Surface tension between outer surface of the shell and exterior media	σ_2	0.005	Pa.m
Elasticity Modulus	G_s	50	MPa

There are many commercially available microbubbles having different properties (shell composition, core gas, diameter etc.) in the literature since 1968. Today, microbubbles are developed to stay prolonged time in the stream without dissolving, and the most common microbubbles used in the studies are listed in Table 3.2.

Table 3.2. Characteristics of top commercially available MBs [40-42].

Agent Name	Manufacturer	Shell	Gas	Dia-meter (μm)	Resonance Frequency (MHz)
Optison	GE Healthcare	Alumin	Octafluoropropane (C_3F_8 or "OFP")	3-4.5	6.21-20.70
Sonazoid	GE Healthcare	Lipid	Decafluorobutane (C_4F_{10})	0.5-3	4.89-67.27
Sonovue	Bracco Diagnostics	Lipid	Sulphur Hexafluoride (SF_6)	2-3	4.89-8.74
Lumason	Bracco Diagnostics	Lipid	Sulphur Hexafluoride (SF_6)	1.5 – 2.5	6.34-13.27
Definity	Lantheus Medical Imaging	Lipid	Perfluoropropane	2-3	4.89-8.74
SIMB1-2	Advanced Microbubbles Laboratories	Lipid	Decafluorobutane (C_4F_{10})	1-2	7.8-21.35
SIMB3-4				3-4	2.95-4.40
SIMB4-5				4-5	2.17-2.95
SIMB5-8				5-8	1.16-2.17
Micro-marker	FUJIFILM VisualSonics Inc.	Lipid	Nitrogen and Decafluorobutane	1-2	8.74-24.06
USphere	Trust Bio-sonics	Lipid	Octafluoropropane (C_3F_8)	0.7-2	8.74-40.78

SIMB1-2, SIMB3-4, SIMB4-5 and SIMB5-8 from Advanced Microbubbles Laboratories, CO, USA was preferred during experiments due to their monodisperse nature. Their size-distributed population are shown in the Figure 3.2. The advantage

of choosing monodisperse microbubbles over polydisperse microbubbles is the intensified echo amplitude in the case of matching resonance frequency of MBs and the imaging bandwidth. Since monodisperse MBs have the larger number of MBs responsive to the imaging frequency than the polydisperse MBs, ultrasound image quality can be improved. At the resonance and the higher frequencies, monodisperse MBs produce stronger echoes whereas at lower frequencies than the resonance frequency polydisperse MBs are more echogenic [43]. Our imaging system was usually operated at 7.8 MHz which is above the resonance frequency of SIMBs according to the Table 3.2 and it can be concluded that use of monodisperse populated MBs was improved our detection sensitivity.

It is worth mentioning that scattering of MBs increase approximately with the fourth power of applied frequency and the sixth power of the bubble radius [29]. Therefore, SIMB4-5 and SIMB5-8 would be more echogenic in the operating bandwidth of L11-5v transducer.

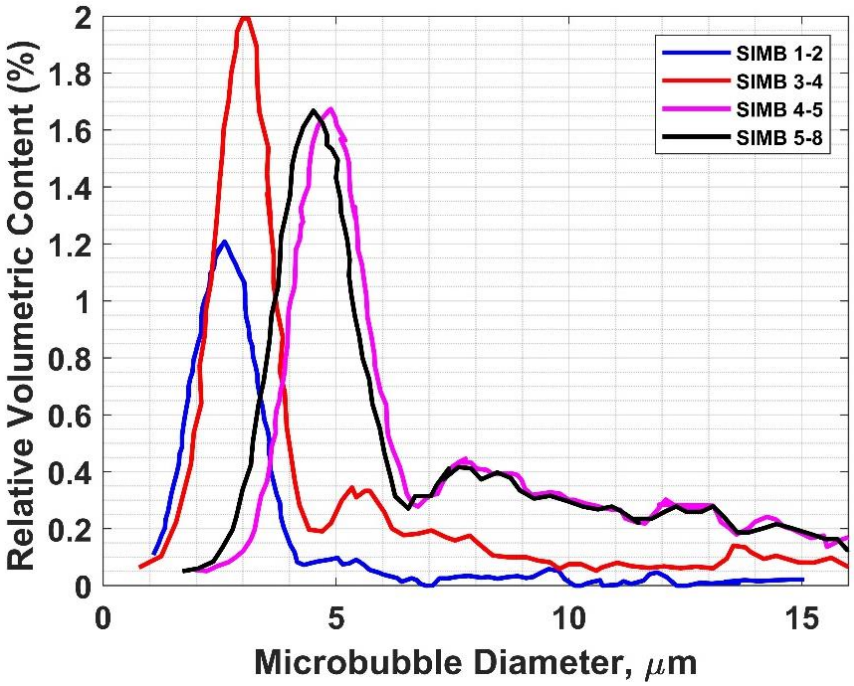

Figure 3.2. Relative volumetric content vs. diameter graphic for SIMBs.

Behavior of microbubbles changes with the magnitude of applied acoustic pressure. Mechanical index (MI) is a measure of acoustic power and informs user about possible damages in the tissue. MI can be calculated as in equation 3.4, where P_- is the peak negative acoustic pressure and f_c is the center frequency of the transducer.

$$MI = \frac{P_-}{\sqrt{f_c}} \tag{3.4}$$

MBs show only linear responses in low MI region. For pressures between 100 kPa and 1 MPa, MBs produce nonlinear oscillation and echo signals differ from incident wave in terms of magnitude and frequency. For pressures higher than 1 MPa, MBs start to destruct as stated with Figure 3.3.

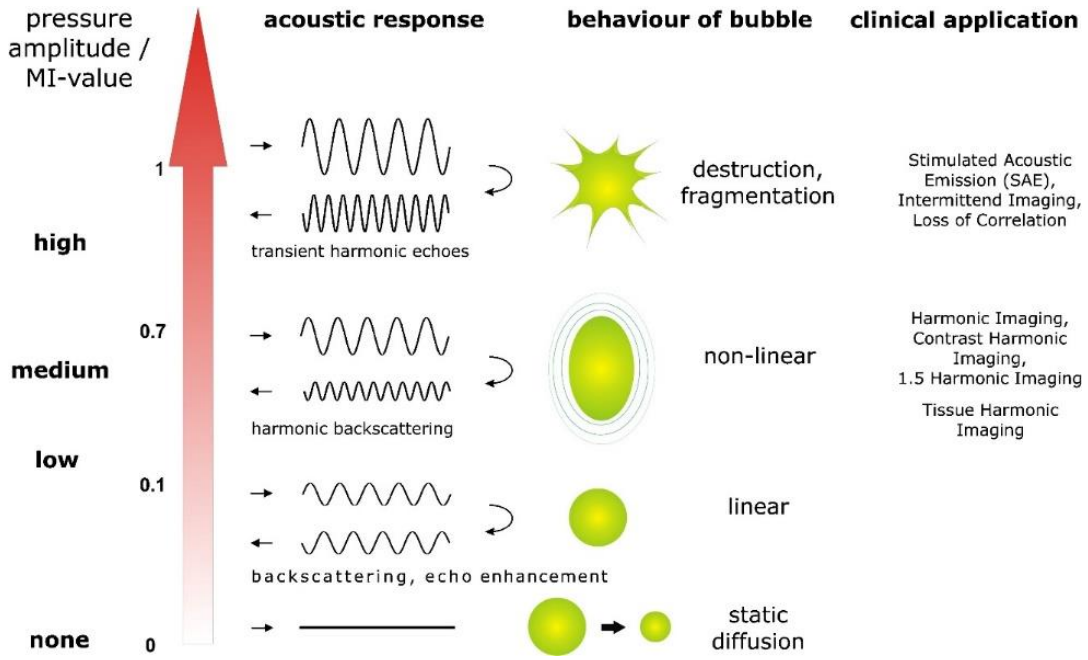

Figure 3.3. Behavior of microbubbles at different mechanical indexes [29].

3.2 Verasonics Vantage System

The Verasonics Vantage System is a flexible research system that is used to transmit, receive, and process ultrasound information. The system consists of two parts which are hardware and the host computer. Hardware includes the necessary parts for transmitting and receiving ultrasound data. Time gain compensation (TGC), 14-bit A/D conversion, digital filtering (FIR) and other signal conditioning tasks are conducted on local memory before data being transferred to the host computer. Then, data stored in the local memory is transferred to the Receive Buffer in the host computer using a DMA (Direct Memory Access) transfer in order to apply reconstruction and display processes.

The sequence of events is programmed by the Matlab Setup script, which creates a binary data file containing all the object structures and programming information stored in the format of Matlab .mat file, when it is executed. A loader application called ‘Verasonics Scipt eXecution (VSX)' is used to load this .mat file into the system, and script in the Matlab environment is run and communication with the hardware is established via a Hardware Abstraction Layer (HAL). Some checks are performed and some attributes needed for programming are added on the structure by the loader program. Both a Graphical User Interface (GUI) and a display window are opened up and control and processing are then handed off to a Matlab External function written in the C programming language, named ‘runAcq’. The sequence of events is then loaded into both the hardware and software sequencers and the execution is started [44, 45].

Table 3.3. Objects defined for collecting data with Verasonics Vantage System

Object	Parameter	Value	Description
PData	PDeltaX, PDeltaY, PDeltaZ	[0.2, 0, 0.2]	Spacing between pixels in X, Y, Z dimensions (λ)
TW	Type	sine	Waveform type definition
	[A, B, C, D]	[7.8125, 0.67, 2, 1]	The central frequency of the transmit pulse (MHz), the duty cycle, number of half cycles, and initial polarity of the burst
TX	Origin	(0,0,0)	Origin of the transmit
	Focus	0	Existance of focusing
	Steer	0	Steering angle for transmits
	Apodization	Ones (128, 1)	Active transmitters
	Delay	Zeros (1, 128)	Delay for transmits
Receive	Apodization	Ones (128,1)	Active receivers
	Start Depth, End Depth	80: 100	Start and end depth values of A/D sampling (λ)
	Apodization	Ones (128,1)	Individual receive channel gain
	# of Acquisitions	7	Number of angles
	Sample Mode	4	(NS200BW)
	Mode	0	The acquisition mode (Replace (=0) or accumulate (=1) RF datin local memory)

Table 3.4. Objects defined for reconstructing images from acquired RF data with Verasonics Vantage System Interface

Object	Parameter	Value	Description
Recon	senscutoff	0.8	Cutoff value for excluding channel from sum.
	RINums	[1:7]	ReconInfo structures associated with this Recon
ReconInfo	Mode	replaceIQ	Replaces data in the InterBuffer
		accumIQ	Accumulates data in the InterBuffer
		accumIQ_replaceIntensity	Replaces the accumulated data in the InterBuffer and ImgBuffer
Process	Processing Gain	1.0	The gain factor to apply to the reconstruction intensity values
	Reject	0	The amplitude level below which the reconstruction output will be mapped to black on the display
	Grain removal	'none'	The 3x3 matrix filter that aims to eliminate single pixels that differ significantly from their neighbors
	Compress method	'power'	Compression method: logarictmic or power
	Display and Display window	1	Writing the processed image data to the Matlab figure window on the screen

3.3 Experimental Setup

The conceptual and the experimental setup are shown in Figure 3.4 and Figure 3.5 with the following items:

1. Host computer with MATLAB (R2020b, MathWorks, Natick, USA),
2. Verasonics Vantage System (Verasonics Inc., WA, USA),
3. Linear array transducer (L11-5v, Verasonics Inc., WA, USA),
4. Tissue mimicking phantom (Agar gel),
5. Syringe Pump (NE-1000, New Era Pump Systems Inc., NY, USA),
6. Microbubble and saline suspension (SIMB4-5, Advanced Microbubbles Inc., USA).

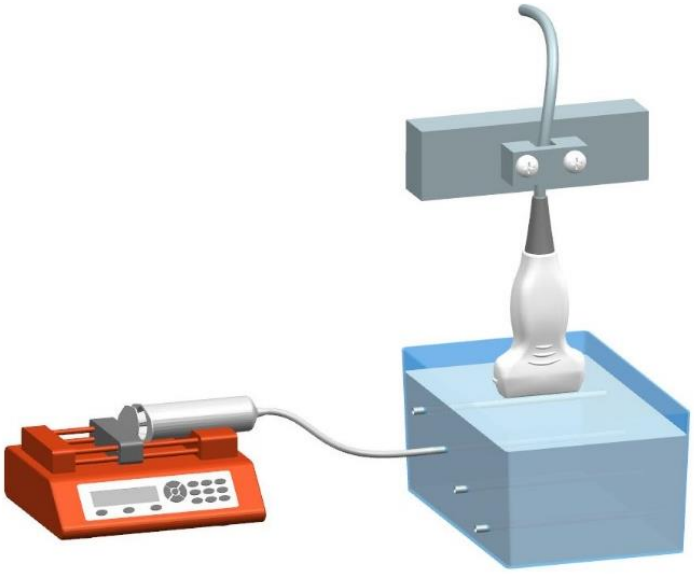

Figure 3.4. Conceptual setup.

Figure 3.5. Experimental Setup.

A syringe pump was driven at 0.5 mL/min flow rate to perfuse vessel tube with diluted MB solution. There are some key points that need to be paid attention while calculating the mean flow velocity. Firstly, vessel diameter should be entered into syringe pump settings. However, minimum allowed diameter is 12 cm. Secondly, syringe that contains the MB suspension has maximum diameter of 3cm and minimum diameter of 1cm at the connection edge of vessel tube. Therefore, another conversion should take place due to the difference between the tip of syringe and the vessel tube diameters.

1. Syringe flow velocity: $V_{syringe} = 0.5\ mL/\min = 88.33\ mm^3/s$
2. Cross sectional area of the tube: $A = \pi.(1.5mm)^2$
3. Volume of the tube: $V = A \times length = A \times (V_{mean} * \Delta t)$
4. Mean flow velocity: $V_{mean} = \frac{V_{syringe}}{\pi.(1.5mm)^2} = \frac{88.33\ mm^3/s}{\pi.(1.5mm)^2} = 11.8\ mm/s$

In human body, blood velocity in arterial vessels are approximately 1 m/s so frame rate should be high enough to catch MBs in a fast blood flow. During compounding plane wave imaging, frame rate of the imaging system was set to 500 fps which refers to 2ms time duration. Although the length of transducer is approximately 38 mm,

region of interest was chosen to cover between -9 mm to +9 mm in lateral direction. Therefore, a single MB travels 18 mm during acquisitions. To capture flowing MB movement regarding full range observation, imaging time of 2s should be allocated. During imaging period (2s), 1000 image frames were captured to be transferred for further processing. During this time period, MBs can travel 23 mm and are located in the region of interest for many frames [46].

3.4 Design of Ultrasound Imaging Sequences

In order to obtain super resolution ultrasound images by localizing MBs, high frame rate (HFR) sequences should be designed. Ultrasound imaging at very high frame rates become possible by using plane waves instead of conventional synthetic aperture acquisitions. As mentioned in Chapter 2.3, use of coherent compounding plane waves will compensate the lack of focusing and help improving image quality while satisfying HFR.

Before explaining sequences step by step, it is worth mentioning some parameters used in the script such as super-frames, number of angles, time between acquisitions.

Before combining ARF and Ultrafast imaging sequences, experiments were conducted only using coherent compounding plane wave (CPCW) imaging in order to detect microbubbles. For this purpose, two scripts are written: first sequence is designed to save ultrafast acquisitions and second script is for offline reconstruction of each acquisitions to create the beamformed IQData or ImgData. Reconstruction process takes longer time than the time between each acquisition so it cannot keep up with ultrafast acquisitions. A save button is created on the GUI-window allowing user to start saving acquisitions.

3.4.1 Coherent Compounding Plane Wave Imaging Sequences

Verasonics provide an example structure of the coherent compounding plane wave imaging script. Users are able to make some changes in the provided flash imaging script to make it more convenient for intended purpose. The adjustments made in the sequence are explained as follows:

1. Collected RF data in the hardware is transferred to host computer by "transferToHost" command. However, it is not possible to fill the RcvBuffer and transfer all frames at the same time with one "transferToHost" command. In other words, each frames must be transferred individually by using this command. It is important to use less number of transfer command since it slows down the frame rate during HFR imaging. Therefore, super frame concept is introduced to transfer more RF data by one transfer command.
2. Another precaution taken not to reduce FR is to apply reconstruction only for the generation of first image of the each super frames.
3. Only the first image from the first frame is reconstructed to generate image during ultrafast imaging between FUS cycles. If reconstruction is applied to all frames in real, the frame rate of the sequence will decrease. Only one image is reconstructed from the super frame in order to see the process in the display window.

After completing all these steps, the script jumps back to the start and repeat until the user presses freeze button. Afterwards, saved RcvData is given to reconstruction script that will apply all acquisitions and generate IQ and image data offline. For reconstruction, RF data in the Receive Buffer needs to go through some processing:

1. Firstly, RcvData is loaded as 3D data (Rows x Columns x Frames). The first acquisition from first frame is reconstructed by "replaceIQData" command into a page in InterBuffer. This command makes IQ data replace the old one if it exists.
2. The other acquisitions that belongs to first frame is reconstructed by "accumIQ" and the last one is "accumIQ_replaceIntensity" command. All

data is written into the same InterBuffer page and hence coherent plane wave compounding technique is applied.

3. After all IQ data is collected in InterBuffer, the predefined process called "ImageDisplay" computes and saves frame into ImageBuffer.
4. These steps are followed for all frames and the resulting images are saved by using external image save function. This process does not save only the raw image data in the ImgBuffer but also the DisplayWindow images. In DisplayWindow images, some post-processing steps are applied by Verasonics system to the raw images.

3.4.2 Imaging and ARF Sequence Design

Many studies that combine long transmit sequences (HIFU) or short duration stimulating (Push) transmits and imaging sequences are introduced in the literature [27-29]. These dual mode sequences are generally used for therapeutic applications. In current applications, two different transducers are used simultaneously so that one transducer is used for destruction/stimulation while the other transducer is used for imaging. Two different transducers can be controlled independently and imaging can be completed without missing any event/frame.

Instead of using two transducers, any stimulating transmits (HIFU/Push/FUS) can be interleaved in between imaging transmits order to implement dual stimulation/imaging sequence. Time-division based and element-division based interleaving are two different methods to design such sequence. As their name implies, time division interleaving transmits destruction pulse and then transmits imaging pulses (or in reverse order) whereas element division interleaving transmits destruction pulse from chosen elements of transducer and imaging pulses are also transmitted at the same time from remaining elements of transducer.

To apply mentioned sequences and evaluate the performance, one must check capability of Verasonics Vantage System. Verasonics provides specification set for transmit signal including frequency, duty cycle, polarity and drive voltage level. The

transmit power controller (TPC) allows to set different transmit voltages for different modes of acquisition. For instance, TPC profile #1 might be used for ultrafast plane wave imaging and TPC profile #2 might be used for FUS transmits. TPC profile #5 is formed to allow user to arrange transmit bursts at high power levels. “Extended Burst” and “External HIFU” options are defined for transmitting high power. The main difference between these options are the source of voltage. Extended Transmit option employs internal supply by charging & recharging the storage capacitor whereas HIFU option uses an external power supply connected to the hardware. To sum up, TPC profile #5 is utilized to select the high-power transmit supply while TPC profiles #1 through #4 can still be used in their normal fashion for imaging. This allows the transmit voltage levels for HIFU bursts and imaging to be controlled completely independent from each other. Transmit burst frequency, duration, active aperture, focus, etc. can also be programmed independently for each transmit burst.

Conventional dual mode methods that use stimulating transmits such as shear wave elastography, acoustic radiation force imaging (ARFI) do not have any requirement about fast switching between destruction and imaging modes. However, in this study the main objective is to use FUS manipulation and ultrafast imaging of MBs simultaneously. Although primary intention is to transmit FUS pulses at high power and imaging pulses at low power, Vantage system capability is not qualified for changing TPC profile fast (i.e. lower than 100 us) or setting different voltage values for each array elements simultaneously. Approximately, $0.5 + \Delta V$ milliseconds is necessary between destruction and imaging transmits. This duration will be insufficient to capture MBs’ movement while system is trying to adjust output voltage from focused to imaging power level.

The problem regarding a rapid voltage profile change is overcame by using a different perspective. Parametric transit waveform is defined by an array [A, B, C, D]. By scaling B parameter which refers to duty cycle of the transmit waveform, one can control maximum transmit voltage of the transmit waveform. Intended sine shaped waveform will be multiplied by square shaped duty cycle waveform to obtain final transmit waveform. When duty cycle is 10 %, rising edge of a sine wave will

be clipped before multiplication amplitude reaches to maximum voltage level. Therefore, imaging transmits have a lower peak-to-peak voltage value than destruction transmits. However, pulse width scaling will result in a small distortion of the transmit focus and phase shift phase of the entire waveform [16]. To measure pulse width scaling effect on peak voltage of transmit waveform, a utility function called "EventAnalysisTool" is used and the results are shown in Table 3.5 in the below.

Table 3.5. V_{peak} transmit voltage used for ARF and imaging transmits.

	Imaging Transmit (Duty Cycle=67 %)	ARF Transmit (Duty Cycle=10 %)	ARF Transmit (Duty Cycle=20 %)	ARF Transmit (Duty Cycle=67 %)
Voltage (V)	10	1.5	2.8	5
	20	3	5.6	10
	30	4.5	8.4	15
	40	6	11.2	20
	50	7.5	14	25

TPC profile change is not used and for both modalities and the transmit voltage of 20 Volts is used. However, due to focusing of stimulation transmit, total power does not spread out the whole region, and hence the total power output directed into the focused area. To prevent excessive power transmit into specific area and destruction of MBs, apodization is reduced from 128 elements to 4 elements located in the center for ARF transmits. Different settings for ARF and imaging pulses such as duty cycle, frequency, number of cycles and presence of focusing are summarized in Table 3.6.

Table 3.6. Transmit pulse properties.

Transmit Waveform	Voltage (V)	Duty Cycle	Frequency (MHz)	# of cycles	Focusing
ARF	20	0.2	3.9	6	+
Imaging	20	0.67	7.813	2	-

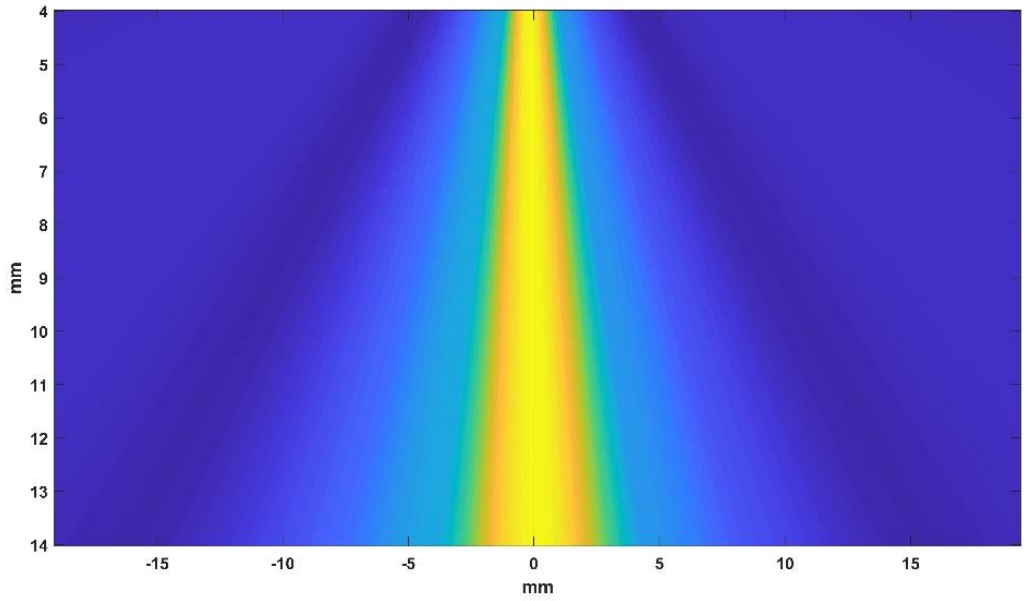

Figure 3.6. Peak transmit intensity map of FUS transmit with four elements.

The imaging sequence with ARF consists of following steps:

1. Script contains two independent sequences so that the results with and without ARF transmits can be obtained experimentally under the same conditions. For this purpose; two receive, inter, image buffers and display windows are created. In addition, a toggle button is generated to trigger second sequence that includes ARF transmits which are intertwined between steering angles.
2. Script starts with coherent compounding plane wave imaging described in Chapter 3.4.1. When "FUS ON" toggle button is pressed, the second sequence starts to run. The first event defined in the second sequence is to transmit the stimulating FUS signal. Time to next acquisition ($TTNA_1$)

between the FUS transmit and the incoming first compounding angle transmit of imaging acquisition is set to 10 µs. $TTNA_2$ between the compounding angle transmits is set to a value that satisfies FR=500 Hz without depending on number of angles (na) used in the sequence.

3. To obtain one image, frame imaging transmits are repeated by the total number of angles. Total time needed for one image frame is calculated by $\left({}^{1}/_{FR}\right) - [TTNA_1 + (na - 1) \times TTNA_2]$. When "FUS OFF" toggle button is pressed, script goes back to first (without ARF transmits) imaging sequence.
4. The working principle of data acquisition algorithm in terms of data transfer and reconstruction processes is the same with the sequence defined in Chapter 3.4.1.

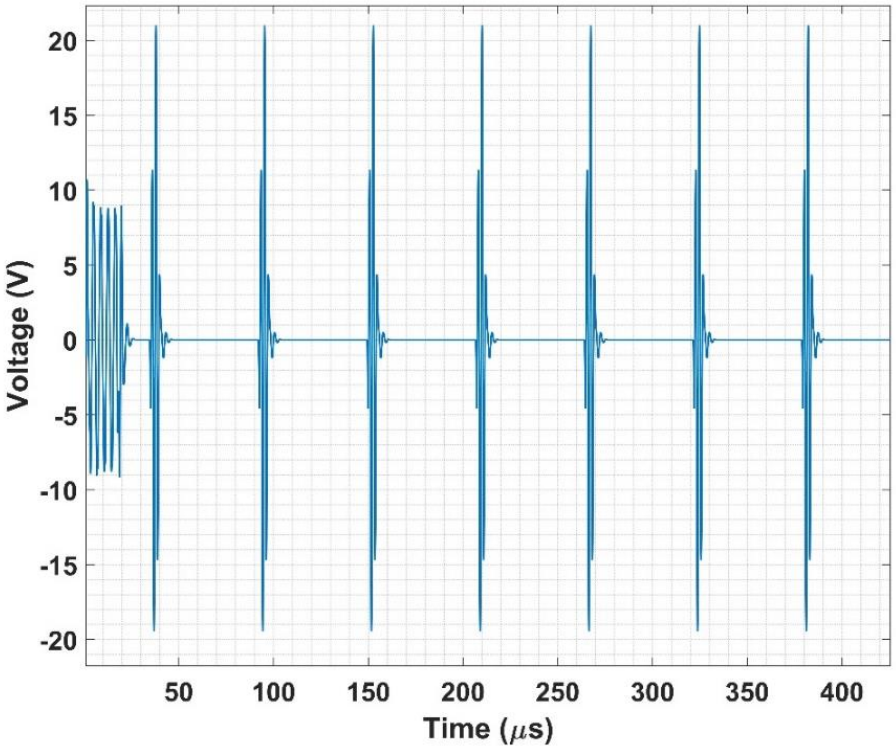

Figure 3.7. Transmit sequence with FUS transmit is added in between imaging frames.

CHAPTER 4

SUPER RESOLUTION IMAGING POST PROCESSING STEPS

Ultrasound localization microscopy (ULM) processing steps are presented in order to detect MBs which are smaller than the diffraction limit. Firstly, general flow of post processing steps are introduced as shown in Figure 4.1. Then, each post processing step is explained in detail and the results after each step are presented through one example acquisition data obtained during experiments.

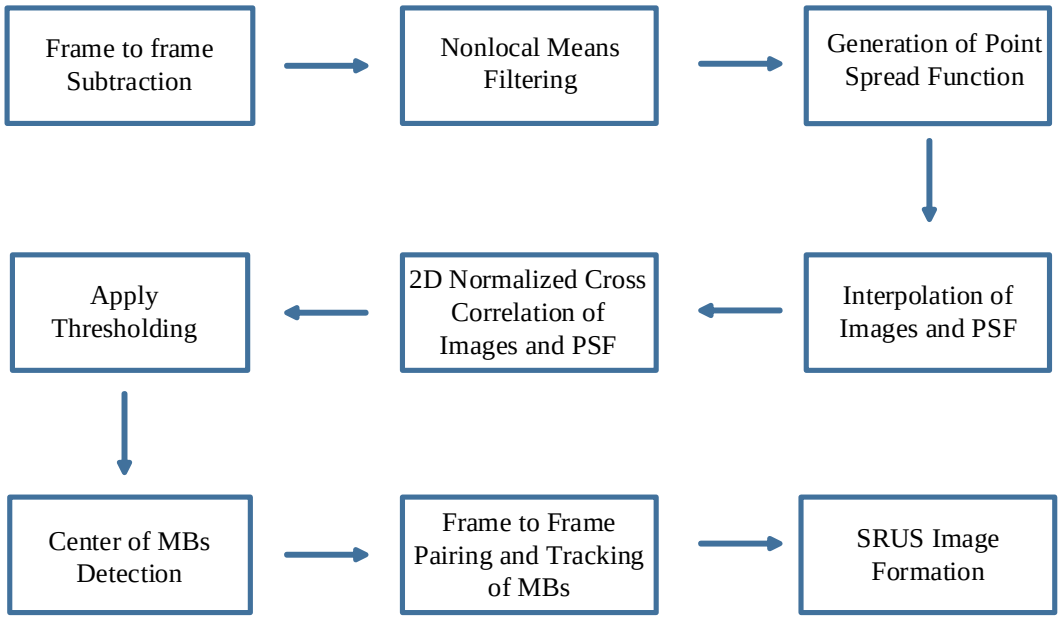

Figure 4.1. Summary of MB detection post processing steps.

Beamformed IQ data can be obtained from experimentally acquired RF data after executing the reconstruction offline. However, in order to detect MBs further post-processing steps are required.

1. In order to obtain blinking MB signals from beamformed in-phase quadrature data, three ways for extraction of MB signals are examined in this study:

a) By differential imaging which refers to subtraction of adjacent frames in order to remove tissue and stationary MB signals.
b) By pulse inversion method which is the process of summing echo signals coming from positive and negative transmit waves, and nonlinear responses can be shown.
c) Spatiotemporal singular value decomposition (SVD) filter can be applied to remove signals from stationary tissue and background noise.

After extracting MB signals, in-phase quadrature datasets are converted to intensity datasets by the square root of the sum of squares. Then, the highlighted microbubble signal is transferred to the next processing step.

2. Second step is de-noising because MBs can easily be confused with the noise. Without causing MB signals blurring, noise should be suppressed. Therefore, non-local means filtering (NLM filter) is decided to be applied [47]. Further noise elimination can be achieved by obtaining the background noise from reconstructed data using lowest singular value.
3. The third steps are the interpolation of both images and PSF to get more accurate results. For this purpose, x8 cubic spline interpolation is applied.
4. At this step, localization of MBs is done by extracting 2D cross-correlation (CC) map of dataset with point spread function (PSF) of an imaging system.
5. Thresholding is applied to filtered 2DCC gray-scale images to convert them into binary images and remove non-essential details.
6. Each MB centers will be marked by local maximum search algorithm. (e.g. "imregionalmax.m" function of Matlab).
7. After detecting individual MBs, tracking algorithms should be used for following MBs at each frame. The most common tracking algorithm is the "Hungarian" which takes the data points in one frame and calculate the weighted average of data points of current frame and the data points of next frame. Then, algorithm creates a match between the data points of frames by choosing the minimum average.

4.1 Background Subtraction

4.1.1 Singular Value Decomposition

Singular value decomposition (SVD) method is applied for clutter filtering purposes by utilizing different spatial and temporal characteristics of tissue and blood. Tissue signals show high spatial correlation whereas blood signals show poor spatial correlation.

Before applying SVD, raw IQ data should be reshaped into a space-time Casorati matrix (S). Each column of Casorati matrix refers to each image frame arranged through time as shown in Figure 4.2. S has $(n_x \text{ x } n_z \text{ , } n_t)$ dimensions where n_x, n_z and n_t are the number of spatial samples along x-direction, z-direction and the number of time samples respectively.

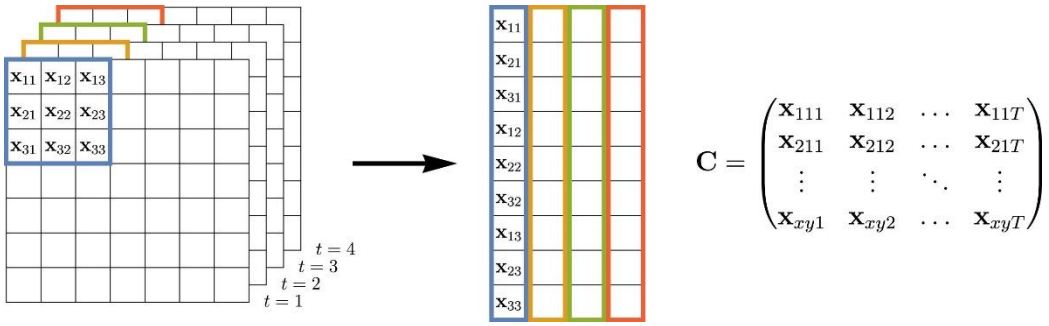

Figure 4.2. The construction of Casorati matrix from image frames [48].

SVD decomposes a rectangular Casorati matrix into three matrices referring spatial and temporal eigenvectors and eigenvalues matrices as shown with Equation 4.1

$$S = U.\Delta.V^* \tag{4.1}$$

Columns of $U$and V matrices correspond respectively to the spatial and temporal singular vectors of S. U and V are orthonormal matrices. Δ is a diagonal matrix and its diagonal elements are singular values. High singular values belong to tissue due to its high temporal coherence and high strength whereas medium singular values

belong to blood due to less temporal coherence. Finally, the lowest singular values belong to noise [48-50].

Spatial coherence of a wave can be defined as changes in wave with respect to distance. In other words, spatial coherence is related with the cross-correlation between two points in a wave for all times. For instance, transmitted plane wave is spatially coherent along the axis that is transverse to the direction of propagation. However, if that wave is reflected by microbubble, the amplitude and the phase are changed at each point and hence the wave becomes incoherent [51].

In ultrasound imaging system, spatial coherence is a measure of the similarity of backscattered echoes received by individual transducer elements at a given time, as a function of element separation. Van Cittert Zernike (VCZ) theorem have described the spatial coherence of ultrasound waves. The theorem predicts the similarity of backscattered pressure field measured by ultrasound transducer as a function of space. According to this theorem, the spatial coherence is the scaled Fourier transform of the intensity distribution of an incoherent source [52].

Temporal coherence is a measure of the correlation of signals at different points along the propagation direction. Temporal coherence can be defined as the measure of the average correlation between the value of a wave and itself, delayed by T (time period of oscillation of the wave) at any pair of times. Temporal coherence can be used to describe how monochromatic a source can be. In other words, it describes the way that a wave can interfere with itself for a certain time period [53].

The key difference between temporal and spatial coherence is that temporal coherence describes the correlation between waves that are observed at different moments in time, whereas spatial coherence refers to the correlation between waves at different points in space, which are either lateral or axial.

Physical meaning of SVD Filter is decomposing the ultrasound data in the form of casorati matrix into a singular values weighted separable matrices, which is the outer product of spatial and temporal singular vectors. This decomposition operation is

mathematically expressed by Equation 4.2 and applied version on ultrasound data as shown with Figure 4.3.

$$S = \sum_i \lambda_i \,.\, A_i = \sum_i \lambda_i \,.\, U_i \otimes V_i \tag{4.2}$$

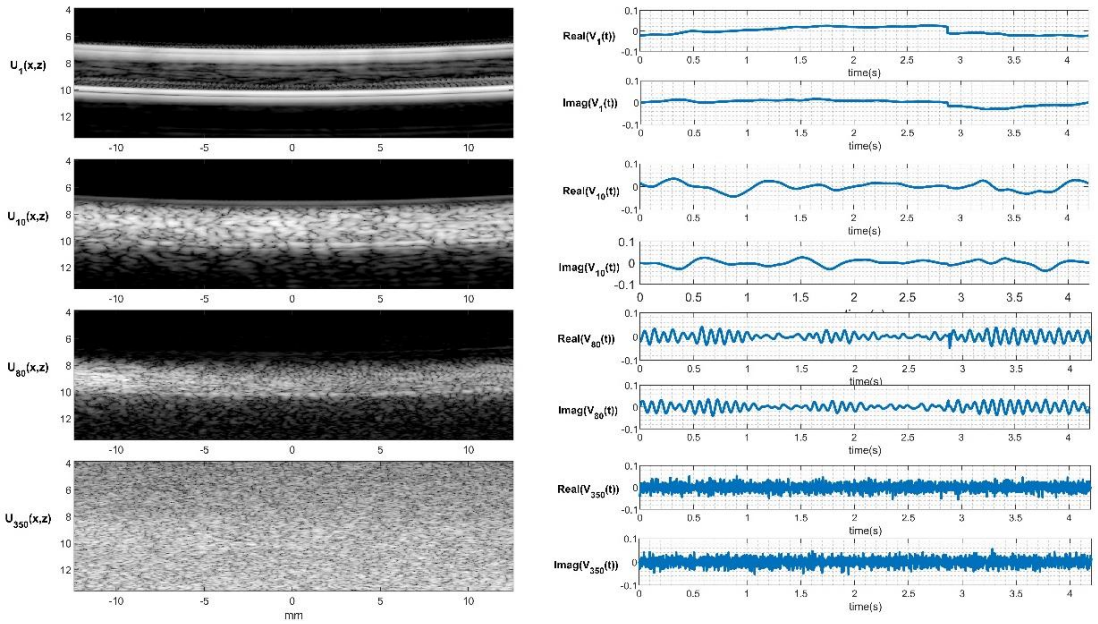

Figure 4.3. Singular Value decomposition of our acquired frames.

SVD requires thresholds as all other filtering operations. After low and high threshold values are found, SVD filtering method eliminates the components that are not in between threshold values or a low-rank matrix projection I_f is designed to be multiplied. After that new U, Δ, V* matrices, depending on which threshold method is applied, are putted into equation to apply inverse SVD calculation. Then, the filtered signal was reconstructed by:

$$signal(x,z,t)_{filtered} = \sum_{i=T_l}^{last} U_i(x,z).\lambda_i.V_i(t) \tag{4.3}$$

After removing the clutter signals, IQ data sets can be converted to the intensity data by the square root of the sum of square. After that, by using external function property of Verasonics Vantage System, raw image data obtained after SVD filtering

can be given as input of image process tool to obtain comparable before and after filtering results.

Performance of eigen-based clutter filtering is closely related with the proper selection of lower and upper thresholds. Threshold values can be estimated by using different properties of output matrices of SVD so that estimations can be grouped in three categories as follows: threshold based on singular values, temporal singular vectors and spatial singular vectors.

4.1.1.1.1 Threshold based on Singular Values

Singular values matrix Δ is obtained by utilizing SVD. First of all, certain threshold value is decided so that singular values above this pre-defined threshold will be rejected. The corresponding dB level is calculated to be used in other sets of data (Figure 4.4, blue dashed line). In other words, magnitude difference between tissue and blood signals is approximately 30 dB [54].

Secondly, the overall signal is an additive combination of a tissue signal and a blood signal. The tissue signal and blood signal have a given backscattered energy. It can then be decided to choose the threshold when the ratio between the cumulative sum of the blood singular values and the overall signal energy, defined as the sum of all singular values (Equation (4.4), reaches a certain (negative) dB level (Figure 4.4, pink dashed line).

$$\frac{\mathrm{Energy_{blood}}}{\mathrm{Energy_{total}}} = \frac{\sum_{k=N}^{\mathrm{Rank(S)}} \lambda_k}{\sum_{k=1}^{\mathrm{Rank(S)}} \lambda_k} \tag{4.4}$$

Another perspective used for singular value based threshold is that singular values are grouped in three regimes in dB scale. First and the highest singular values are belong to highly coherent tissue signals whereas the lowest singular values are belong to noise showing Marchenko-Pastur distribution. Therefore, blood flow containing MB signals are located in between these aforementioned regions. The tissue rejecting high order threshold is chosen as the first turning point of the singular

value curve (Figure 4.4, blue dashed line), given by the first local minimum of the curvature radius. On the other hand, the noise rejecting low order threshold is chosen as the first deviation point of the linear fitted line of the lowest singular value curve (Figure 4.5, blue dashed line). Before and after Singular Values based Threshold SVD filter results are shown in Figure 4.6.

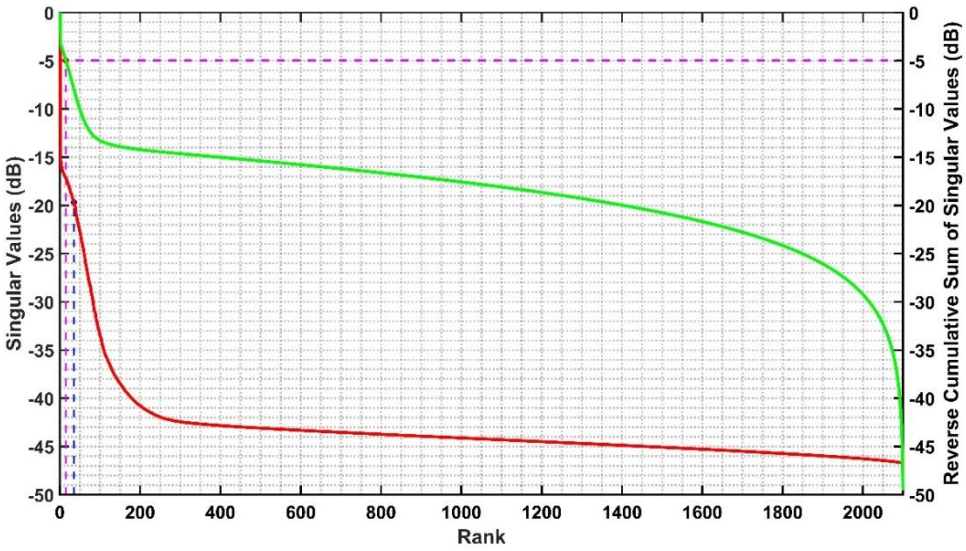

Figure 4.4. Clutter rejecting high order singular value threshold.

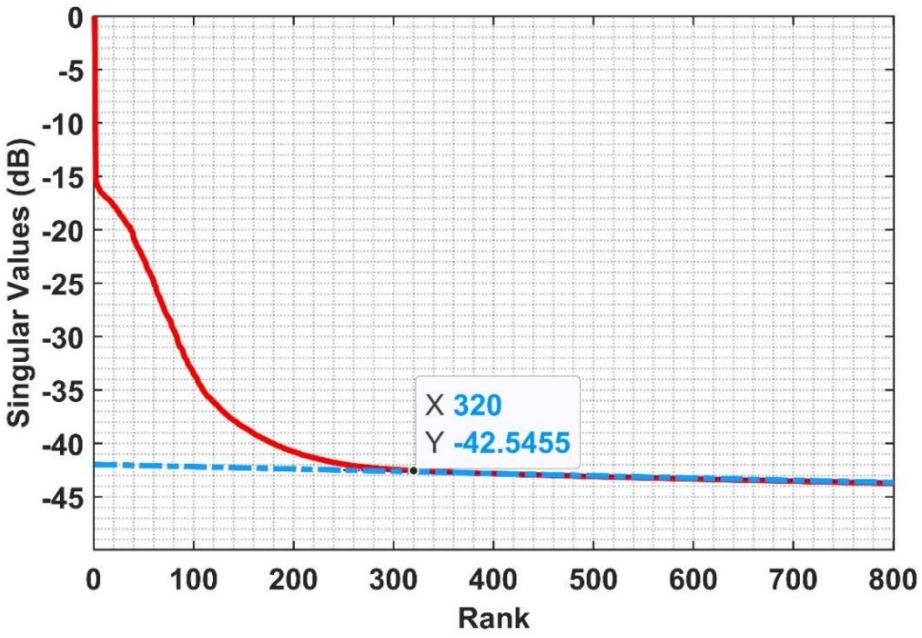

Figure 4.5. Noise rejecting low order singular value threshold.

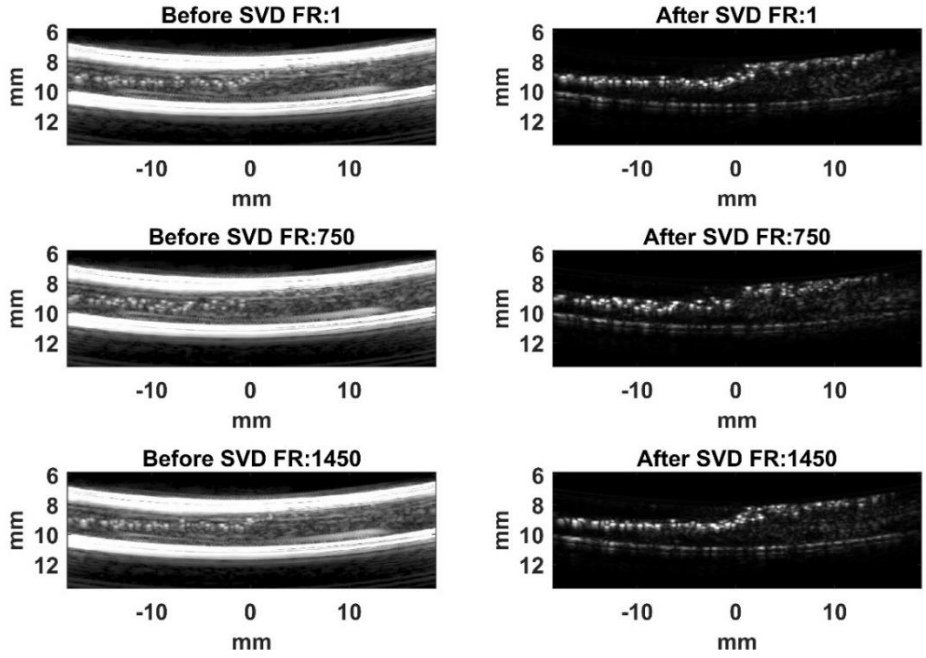

Figure 4.6. Before and after SVD based on singular values based threshold.

4.1.1.1.2 Temporal Singular Vectors based Threshold

For the temporal singular based threshold, the Fourier transform of the temporal singular vectors V* is calculated as shown in Figure 4.7. The tissue motion frequency should be known to implement this threshold method so that the frequency values that cannot exceed the tissue frequency are eliminated.

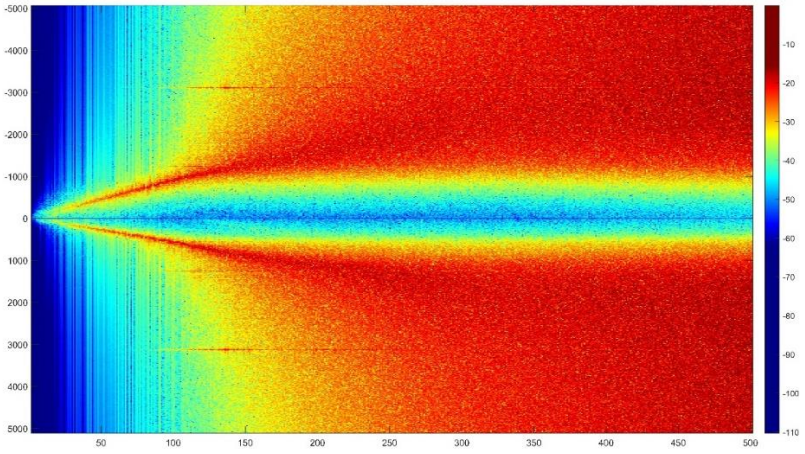

Figure 4.7. Temporal Singular Vectors Power Spectrum Density.

4.1.1.1.3 Spatial Singular Vectors based Threshold

For the spatial singular based threshold, the autocorrelation matrix of the spatial singular vectors U is calculated as shown in Figure 4.8. Due to the difference in spatial characteristics of tissue, blood and noise, different subspaces are revealed.

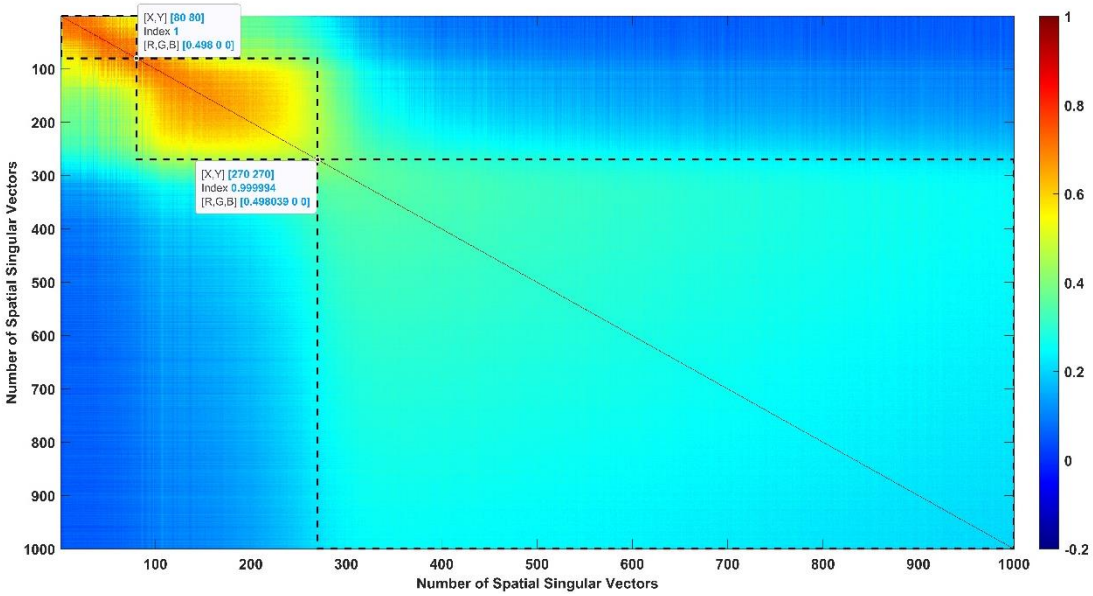

Figure 4.8. Correlation Matrix of Spatial Singular Vectors.

4.2 De-noising

After background subtraction, microbubble localization will take place. However, in order to minimize a false detection of MBs, an intermediate denoising step is introduced. There are many spatial domain filters in the literature such as mean filter, Wiener filter, median filter in which all pixels of an image are used for averaging.

Non-local means is an algorithm in image processing for image denoising. Unlike "local mean" filters, which take the mean value of a group of pixels surrounding a target pixel to smooth the image, non-local means filtering takes a mean of all pixels in the image, weighted by how similar these pixels are to the target pixel. This results in much greater post-filtering clarity, and less loss of detail in the image compared with local mean algorithms.

The non-local means algorithm replaces the value of a pixel by an average of a selection of other pixels' values: small patches centered on the other pixels are compared to the patch centered on the pixel of interest, and the average is performed only for pixels that have patches close to the current patch. As a result, this algorithm can restore well textures, that would be blurred by other denoising algoritm.

$$NL(i) = \sum w(i,j).v(j) \tag{4.5}$$

where, NL(i) is the output of NL-means filter of any pixel 'i', and w(i,j) is the weight depends on similarity between pixels i and j. Similarity between two pixels is measured in terms of similarity (s(i,j)) between their neighborhood.

$$s(i,j) = e^{\frac{-d^2}{h^2}} \tag{4.6}$$

where d is the weighted Euclidian distance between neighborhoods of pixel 'i' and h is the degree of filtering.

Nonlocal Means Filter (NLM) Procedure:

1. Select a pixel i (shown in blue color)
2. Similarity window is shown in green color (7x7)
3. Neighborhood of pixel i (shown in orange accent color)
4. Pixel j (yellow color)
5. Neighborhood of pixel j (shown in red color)
6. Then, s(i,j) for this set of (i,j) is calculated and j is changed
7. Once all s(i,j) is calculated, then calculate w(i,j)

where *w(i,j)* is expressed as follows:

$$w(i,j) = \frac{s(i,j)}{\sum_j s(i,j)} \tag{4.7}$$

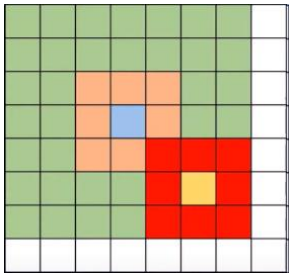

Figure 4.9. NLM Configuration.

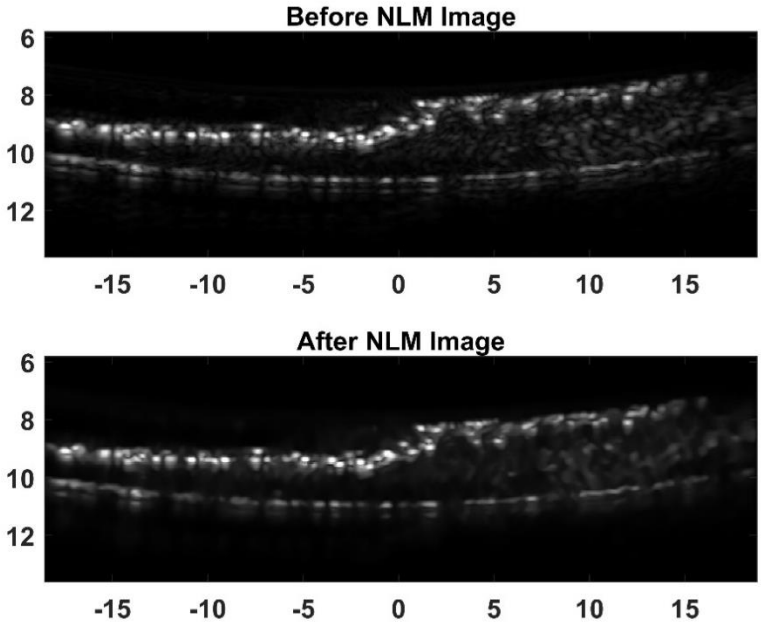

Figure 4.10. Before and after non-local means filter application.

4.3 Microbubble Localization

Microbubble localization can be done with many different ways. However, in this thesis, 2D Gaussian fitting method is used. MBs show Gaussian profile and by looking the correlation of this Gaussian profile and the image, center of MBs can be found.

4.3.1 Point Spread Function

The point spread function (PSF) is the impulse response of an imaging system to a single point source. During generation of images, objects and PSF are convolved so deconvolution of an image and PSF process would reveal the original image without system response. On the other hand, spatial resolution of an imaging system is characterized by the full width half maximum (FWHM) which is derived from PSF.

PSF of an imaging system can be obtained experimentally by imaging a very thin metal wire acting like a point source. However, in this thesis, Verasonics simulator

was used to extract PSF of an imaging system. The user can insert a point source at desired depth and location in the simulation mode. Using the same imaging settings used in experiments, i.e. depth, sense cutoff, pixel spacing in axial and lateral axes, a point source would have seen as shown in Figure 4.11.

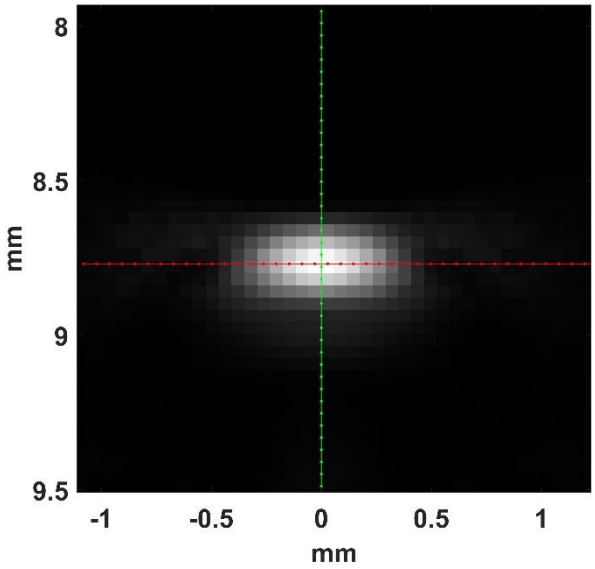

Figure 4.11. Display of single point source.

PSF shows 2D Gaussian distribution and in order to convert this image data to distribution data, 2D Gaussian fitting is applied by using the equation 4.8.

$$PSF = exp\left(-\left(\frac{(z-c_z)^2}{2{\sigma_a}^2} + \frac{(x-c_x)^2}{2{\sigma_l}^2}\right)\right) \tag{4.8}$$

where $(z,\ x)$ are the pixel coordinates and $(c_z,\ c_x)$ are the center position of the generated PSF. σ_a and σ_l represent the average full width at half maximum (FWHM) of MBs in axial and lateral directions, respectively. The average FWHM for each direction can be measured by selecting some MBs from different depths. The average FWHM of PSF in axial and lateral direction is measured to be 276 and 508 μm respectively as shown in Figure 4.12 [51].

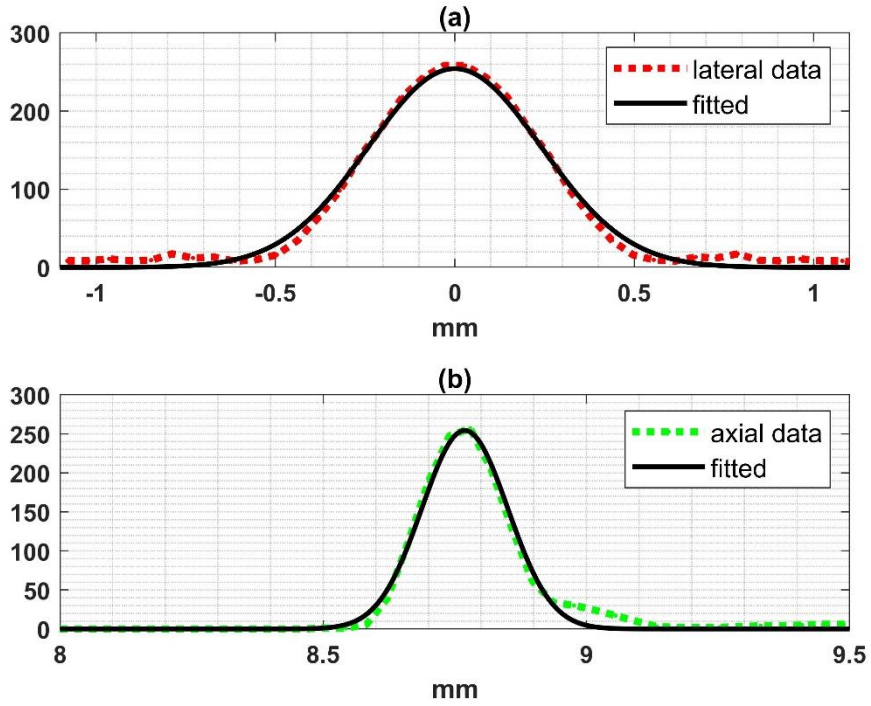

Figure 4.12. Lateral Gaussian fitting, (b) axial Gaussian fitting to point source at 80λ depth.

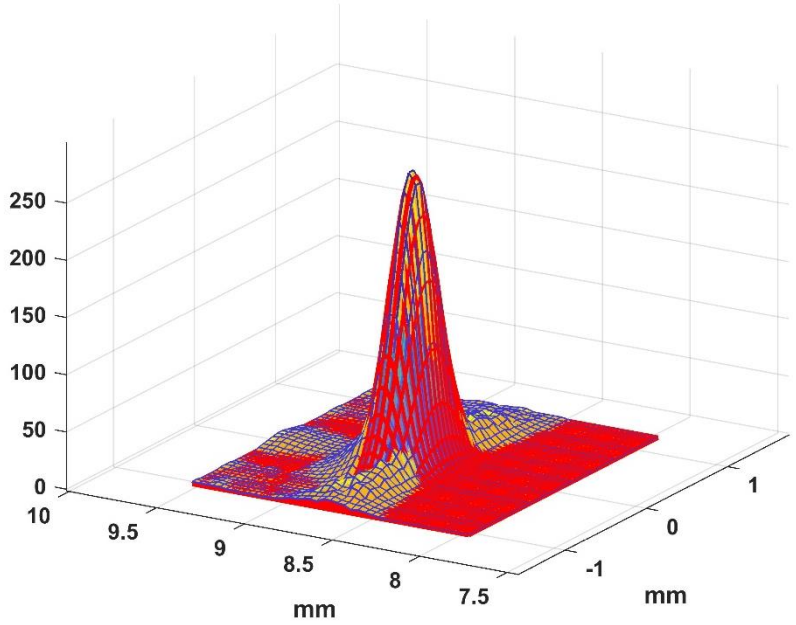

Figure 4.13. 3D Gaussian fitting to point source at 80λ depth.

4.3.2 Interpolation

Interpolation works by using known data to estimate values at unknown points. Common interpolation algorithms can be grouped into two categories: adaptive and non-adaptive. Adaptive methods change depending on what they are interpolating (sharp edges vs. smooth texture), whereas non-adaptive methods treat all pixels equally.

To add precision to the localization, PSF and the MB images were magnified by a factor of four using cubic spline interpolation during post processing. PSF before and after the application of cubic spline interpolation are shown in Figure 4.14.

As an interpolation method, cubic spline interpolation is preferred due to their two main advantages. First of all, interpolation polynomials show oscillatory behavior as their degree increases. However, cubic spline interpolation overcomes this problem and provide smooth interpolation. Secondly, cubic spline interpolation covers 2D area unlike conventional row wise or column wise interpolations. Therefore, each set of interpolation points help rectifying the previously calculated values with minimum error [55].

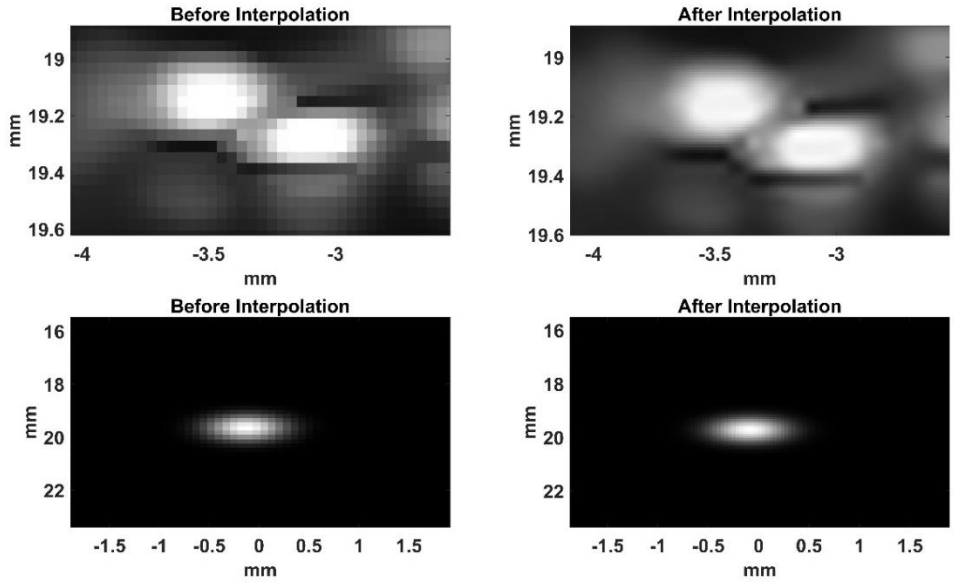

Figure 4.14. Before and after interpolation process.

4.3.3 2D Cross Correlation Map Extraction

2D cross correlation is applied between interpolated images and the generated PSF in order to localize MBs. The idea is that areas in the images that show similar characteristics with PSF were considered as MBs.

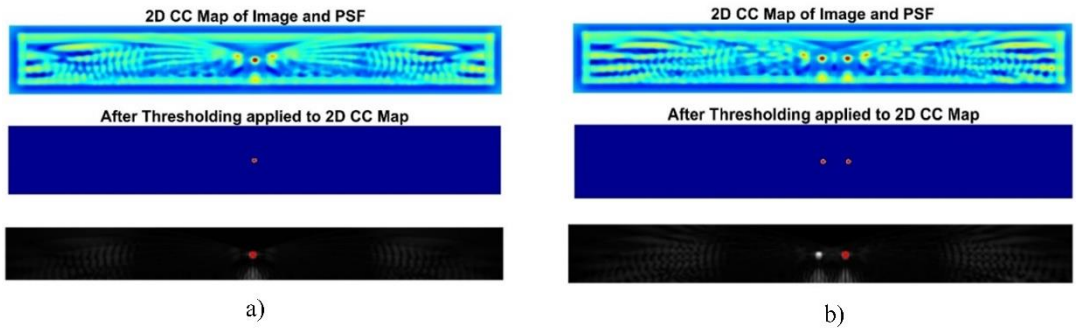

Figure 4.15. Final localization result of (a) one point source, (b) two point sources separated by 10λ.

4.4 Frame to Frame Pairing and Tracking

A simple tracking algorithm is implemented in Matlab. Tracking is basically done by re-creating the trajectories of one or several particles as they move along time. Their position is reported at each frame, but particle identity is yet unknown since which particle in one frame matches to another particle in the previous frame is not known. Tracking algorithms deal with this issue.

In the tracker that is used, links between particles in different frames are created with the help of hungarian algorithm. The hungarian algorithm can associate a particle from one frame to another, based on a weight score. After an iterative process, it is ensured that the sum of the pair of distances is minimized over all of particles between frames [56]. An example of this pairing and tracking algorithm is shown in Figure 4.16.

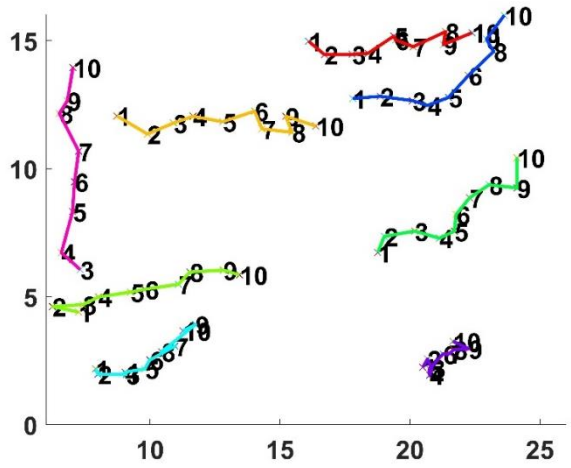

Figure 4.16. Example of Hungarian based tracking method with random points

4.5 Super Resolution Image Generation

It is not possible to spatially separate MBs closer than the FWHM in axial and lateral directions calculated. To obtain super-resolution image, the individual MB localization-based algorithm was applied [57]. In the presented technique, temporal analysis of individual MBs is used to distinguish spatially overlapping images of each MBs. The algorithm applies as follows:

1. Fit a 2D Gaussian function to the MBs in the image I(i,j) using least squares optimization yielding the detected coordinates xc, zc.
2. Find the uncertainty of the position σx and σz temporally using huge number of image frames thanks to ultrafast acquisition.
3. Convert images into super resolution images by using new smaller deviated Gaussian profile during fitting process.
4. Combine the high resolution images $I_{new}(i,j)$ for all MBs into a composite image by summing them.

Detected MBs are rendered into a new spatial domain by using the advantage of being temporally seperable sources. Instead of much larger deviation, MBs can be detected in a smaller deviation temporally. Finally, all images are assembled into one super-resolution image using the MIP method after intensity normalization.

CHAPTER 5

ULTRASOUND IMAGING RESULTS

Ultrasound imaging results obtained by applying preprocessing and postprocessing steps on our experimental data are presented. Firstly, results from ultrafast coherent compounding imaging are presented. In this set of experiment, final super resolution ultrasound image is obtained. Secondly, results from imaging under ARF effect are examined. Pre-processing steps of differential imaging and SVD filtering are compared in terms of correctly detected number of MBs. In addition, population distribution of MBs in the effect of ARF is revealed. Finally, by using third experimental dataset, CNR and CTR values are compared for B mode and pulse inversion method for second harmonic, ultra harmonic and sub harmonic regions.

5.1 Coherent Compounding Plane Wave Imaging Results

Ultrafast ultrasound imaging experiment was conducted by using coherent compounding plane waves with seven angles starting from -10^{o} to $+10^{o}$ degrees. Flow speed was set to 5 mm/s, and SIMB5-8 was used. Frame rate was set to 1000 fps and 3500 images were obtained in 3.5 seconds. As shown in Figure 5.1, ULM techniques were applied and MBs were successfully detected. Tracking algorithm was applied to centers of detected MBs, and extracted MB trajectories are shown in Figure 5.2. Three samples of MB trajectories are selected from Figure 5.2 and their motion is clearly shown in Figure 5.3.

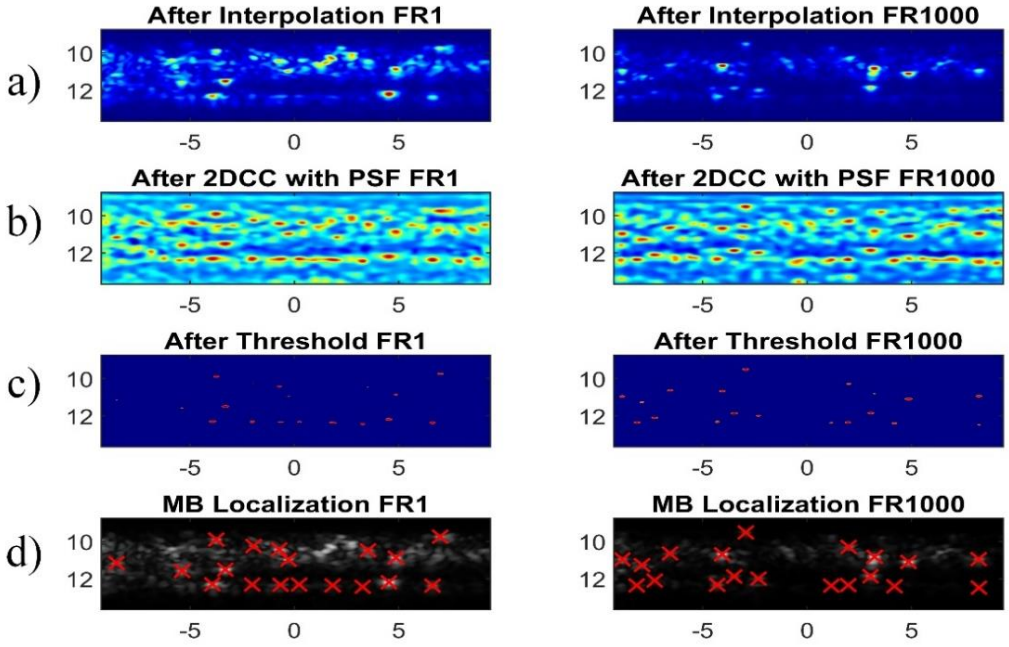

Figure 5.1. Summary of post processing steps of MB detection in frame #1 (FR1) and #1000 (FR1000). (a) Images after SVD filtering. (b) Images after 2D-CC with PSF. (c) Images after threshold process. (d) Localization of MB centers.

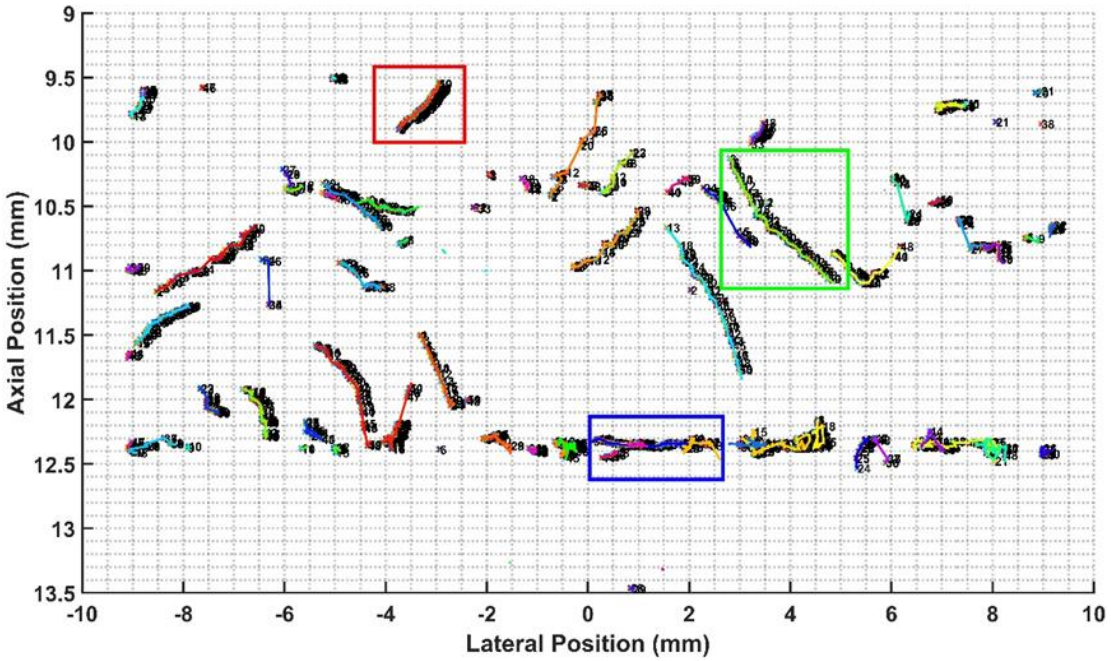

Figure 5.2. MB Trajectories obtained from CPCW imaging sequence

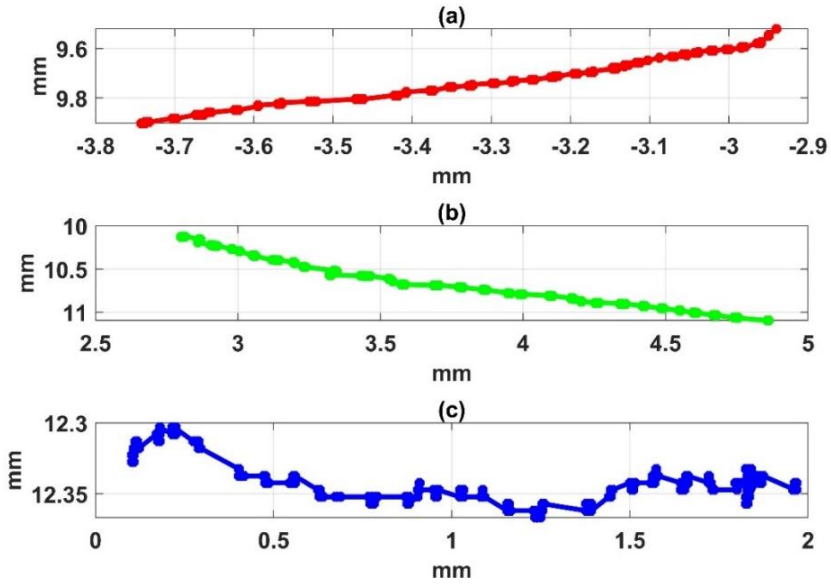

Figure 5.3. Selected MB trajectories of a) MB-1, b) MB-2, and c) MB-3.

Axial and lateral velocities of the selected of the MBs were extracted in Figure 5.4. MBs are freely circulating in the flow under ultrafast imaging. The axial velocity of MB-3 is close to zero since its movement is guided by the wall of the capillary tube. However, MB-3 has the highest velocity in lateral direction due to flow speed. Lateral speed of MB-1 and MB-2 are experimentally found as 2 mm/s.

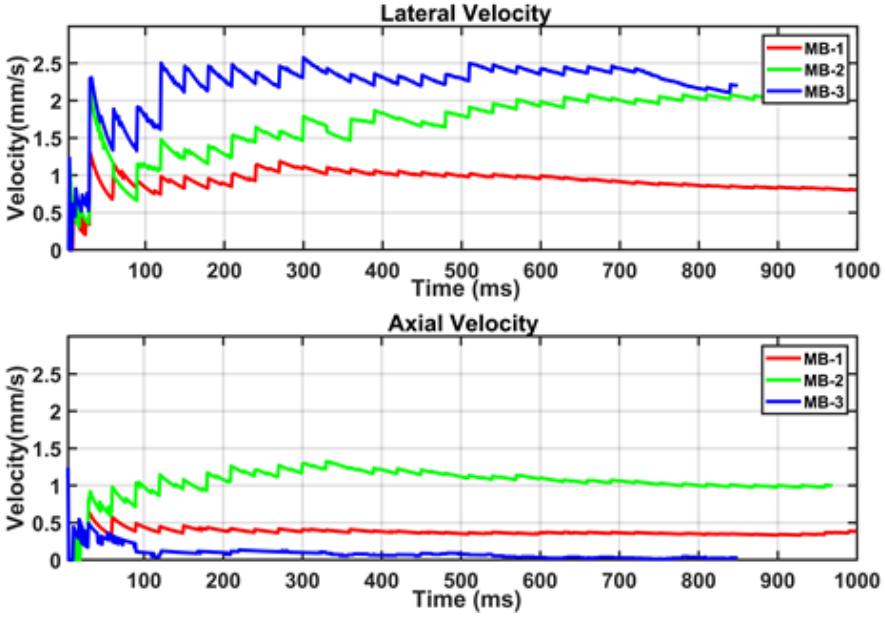

Figure 5.4. Axial and lateral velocity of selected MBs.

The final step would be the generation of super resolution image. Tracking algorithm allows to obtain center positions of individual MBs through time. SRUS technique uses temporal variation of the centers as a new standard deviation for the Gaussian profile that characterizes the system resolution. The final SRUS image of our experimental data is shown in Figure 5.5.

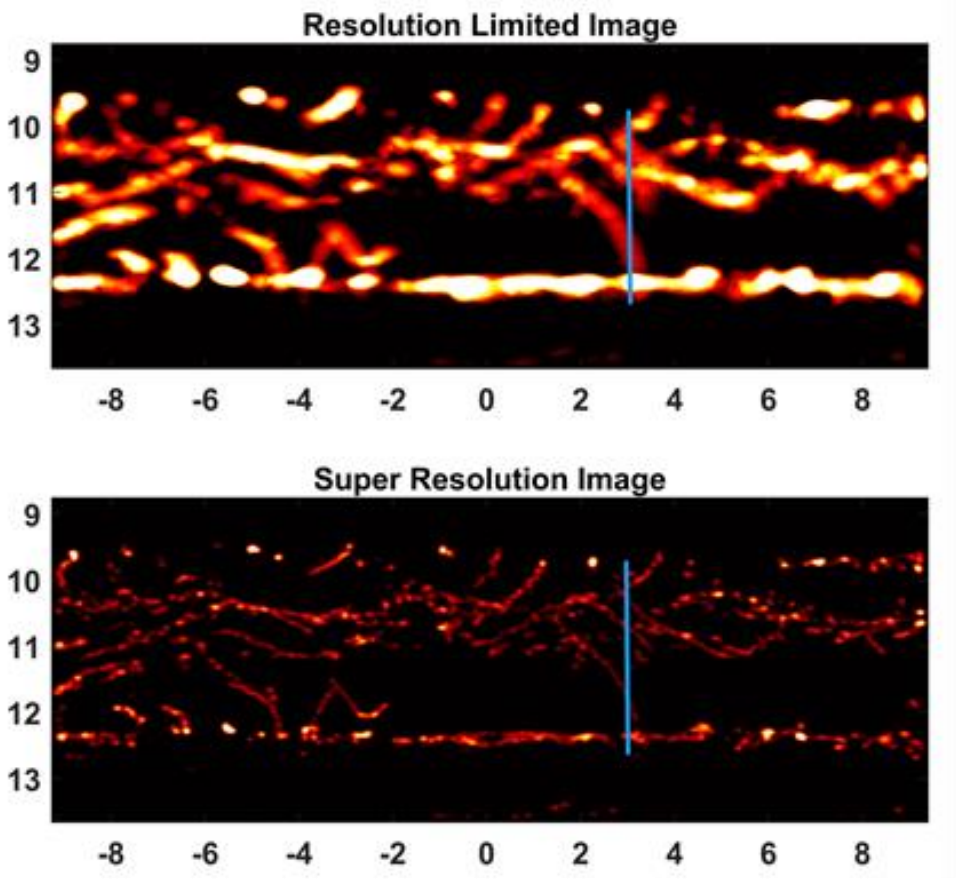

Figure 5.5. Temporally summed images of our experimental data before and after the application of SRUS techniques.

Normalized intensity data of resolution limited and super resolved images on the line indicated with blue in Figure 5.5 was extracted for better understanding of improved spatial resolution. The intensities of cross sections are plotted with respect to axial direction as shown in Figure 5.6. FWHM value is decreased from 214 μm to 79 μm after ULM applications.

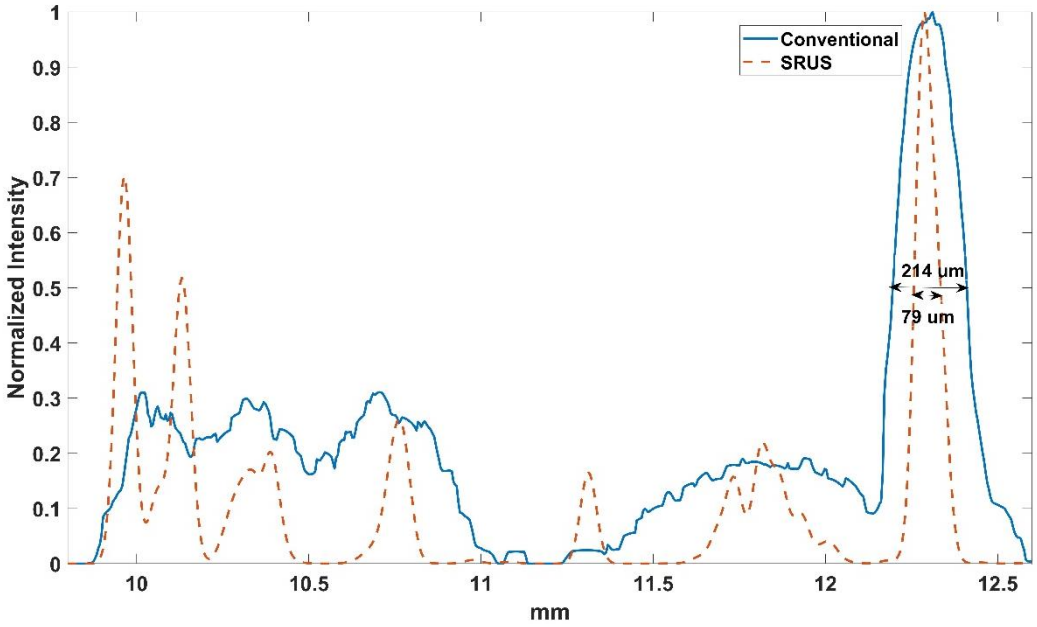

Figure 5.6. Resolution measurement at axial region indicated by the blue line on the previous resolution limited and super resolution image.

5.2 Ultrafast Ultrasound Imaging with Acoustic Radiation Force Results

The results presented in this section were obtained by adding FUS transmits in between CPCW imaging frames. Flow speed is 10 mm/s, and SIMB4-5 was used during these experiments. Transmit voltage was set to 50 V for both imaging and FUS transmits. Frame rate was set to 500 fps and 3000 images were obtained in 6 secs.

5.2.1 MB Detection Performance with DI and SVD Methods

The performance of differential imaging and SVD filtering are presented in this section. FUS transmit was applied between each image frames to be used as effective ARF to push MBs downward direction. As it can be seen from the results, MB flow is through to –x axis direction and FUS is applied at a position of x=0, y=8.5 mm. To generate FUS transmits, central four elements were used to push them in depth without destructing MBs. FUS transmit was formed as a sine wave with a duty cycle

of 0.67 and 5 full cycles. On the other hand, seven coherent compounding angles were used to generate ultrafast ultrasound images (See Table 3.6).

MB detection steps with starting with SVD and DI methods used for background subtraction are presented in Figure 5.7 and Figure 5.8 respectively. MB localizations with 30 frames with a step size of 50 frames (total 1500 frame data are acquired) obtained from DI and SVD methods are plotted together.

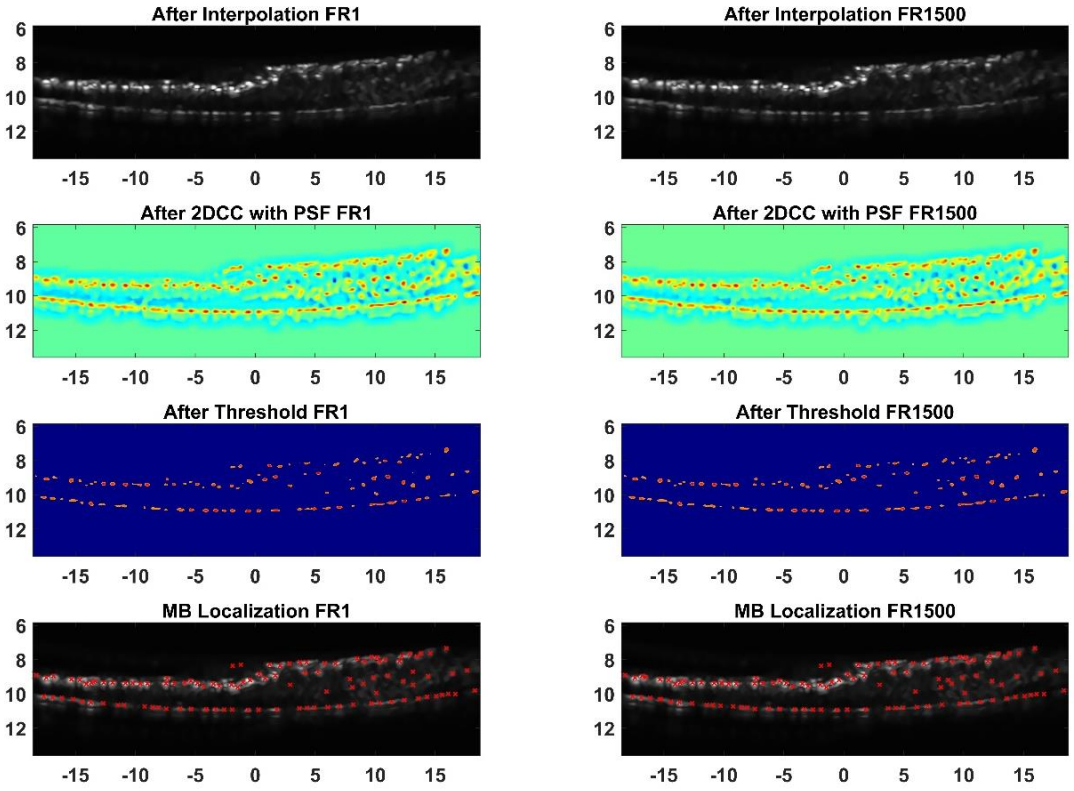

Figure 5.7. MB localization with SVD filtering method.

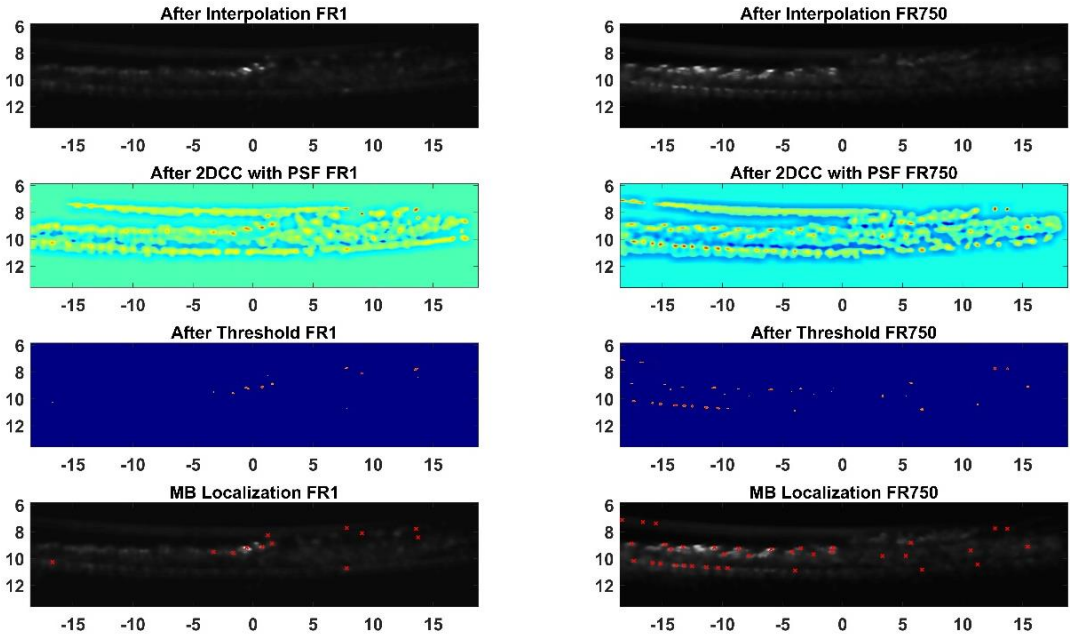

Figure 5.8. MB localization with differential imaging method.

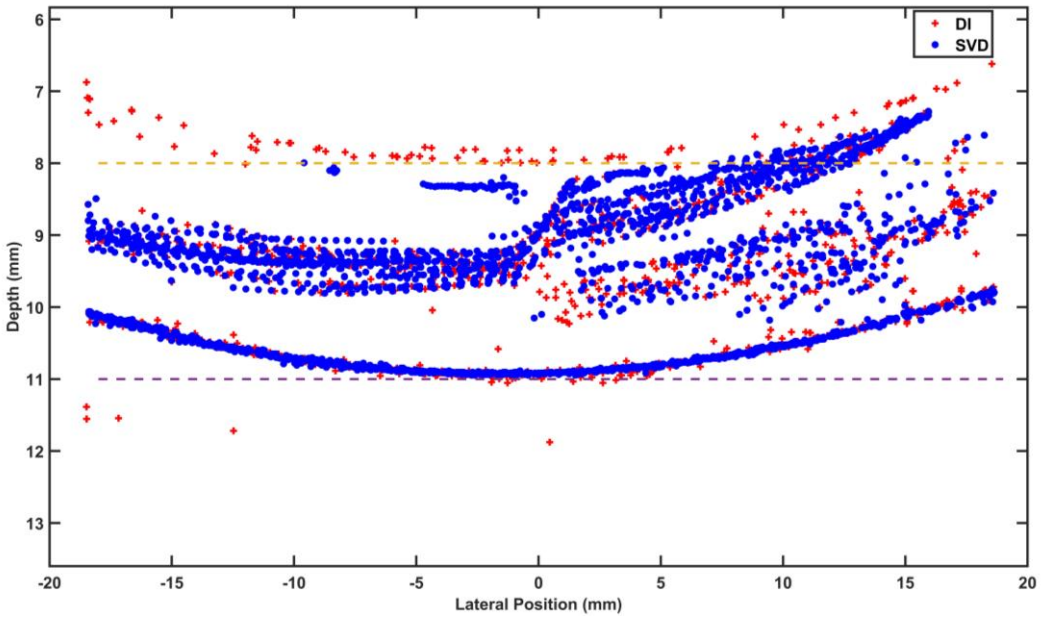

Figure 5.9. MB localizations with 30 frames obtained from DI and SVD methods.

DI is computationally cheaper process but false and less MB detections can be obtained. In Figure 5.9, it is clear that DI causes false detection of MBs more than

SVD filter. There are DI-based detected points residing the outside of the capillary tube and these points can be categorized as false detected MBs.

In addition, position histogram for axial and lateral directions are shown in Figure 5.10. It reveals how MBs are precisely being directed by ARF and the flow since there is a sharp position change in axial direction at x=0 point.

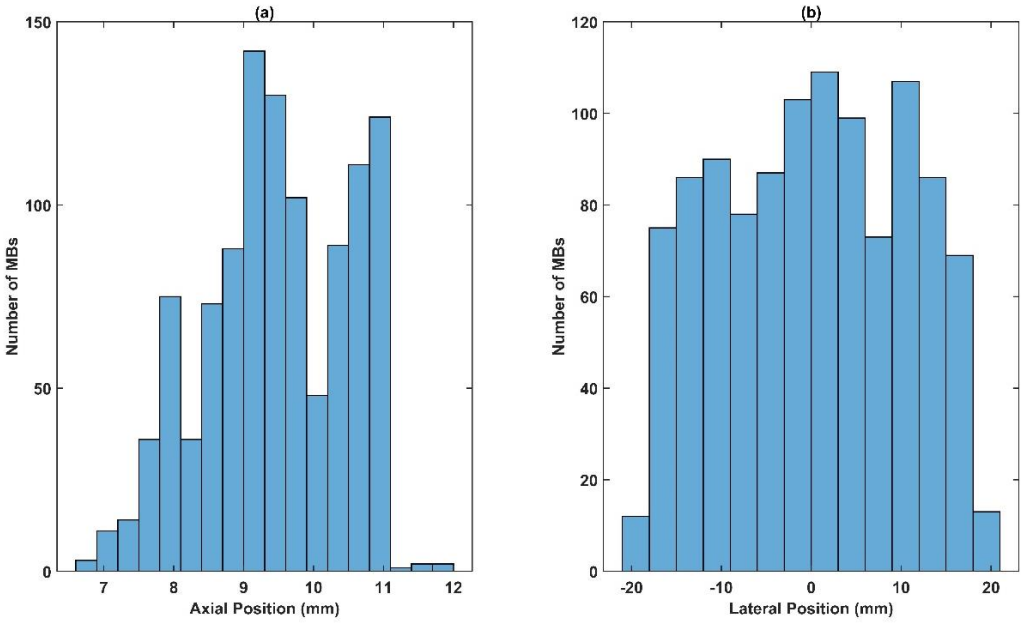

Figure 5.10. Histogram of detected MBs in (a) axial position, (b) lateral position.

5.2.2 ARF and Flow Speed Relation Results

In this chapter, flow speed and ARF relation is investigated as shown in Figure 5.11. The red points represent centers of MBs flowing with a 5 mm/s speed whereas blue points represent centers of MBs flowing with a 10 mm/s speed in a capillary tube.

If the flow velocity is high enough, ARF would not push MBs to interact with the bottom surface of the capillary tube. However, when the flow velocity is lower, push effect of ARF transmits becomes more dominant and more MBs can reach the bottom of the tube.

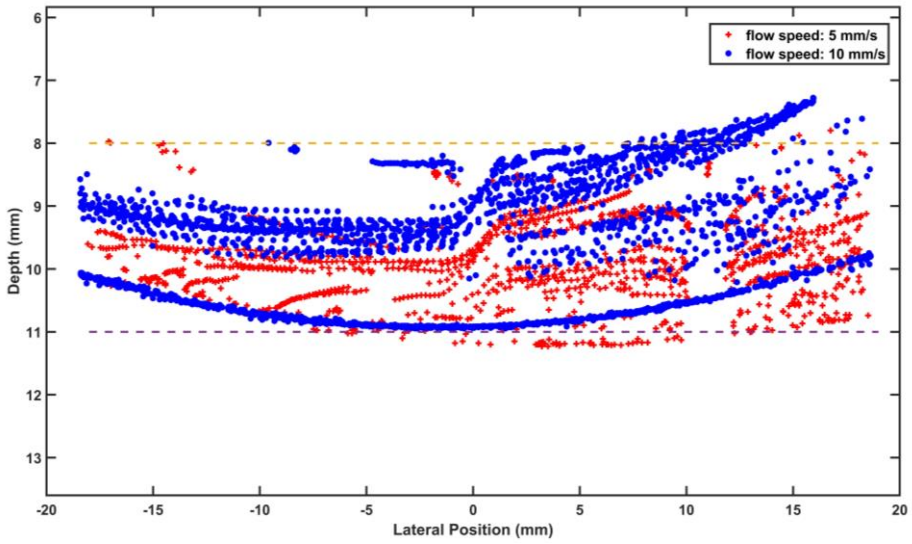

Figure 5.11. MB localizations with 30 frames by a step size of 50 frames obtained from flow speed 5 mm/s (red) and 10 mm/s (blue).

As shown from Figure 5. 12, when the flow speed is higher, more number of MBs are detected in the same time interval. On the other hand, when the axial position of MBs are examined, the peak MB density of blue bars are located in 10 mm depth whereas orange bars are located in 9 mm. Therefore, the slower flow speed results in less number of detected MBs but more axial displacement of MBs.

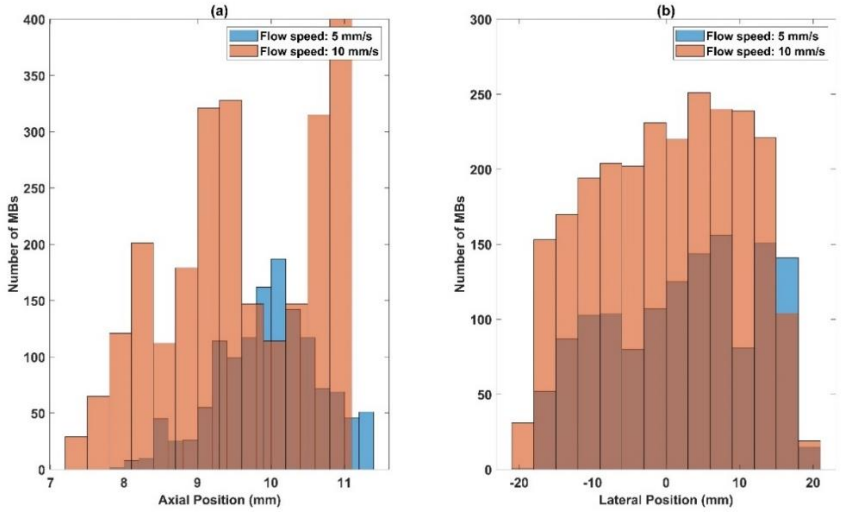

Figure 5. 12. Histogram of detected MBs in (a) axial position, (b) lateral position for flow speed of 5 mm/s and 10 mm/s.

5.2.3 MB Population Distribution under ARF

In this set of experiments, ARF is applied in between compounding angles of each image frames in contrast to results presented in chapter 5.2.1. Flow speed was 10 mm/s and SIMB4-5 was used during these experiments. Transmit voltage was set to 30 Volts for both imaging and FUS transmits. FUS transmits were applied by using one element of the linear transducer located in the center. FUS transmit was formed as a sine wave with 0.67 duty cycle and 5 full cycles. Figure 5.13 shows MB movements under effect of ARF belonging to different times. It is clear that ARF applied at x=0 pushes MBs in the bottom of the tube.

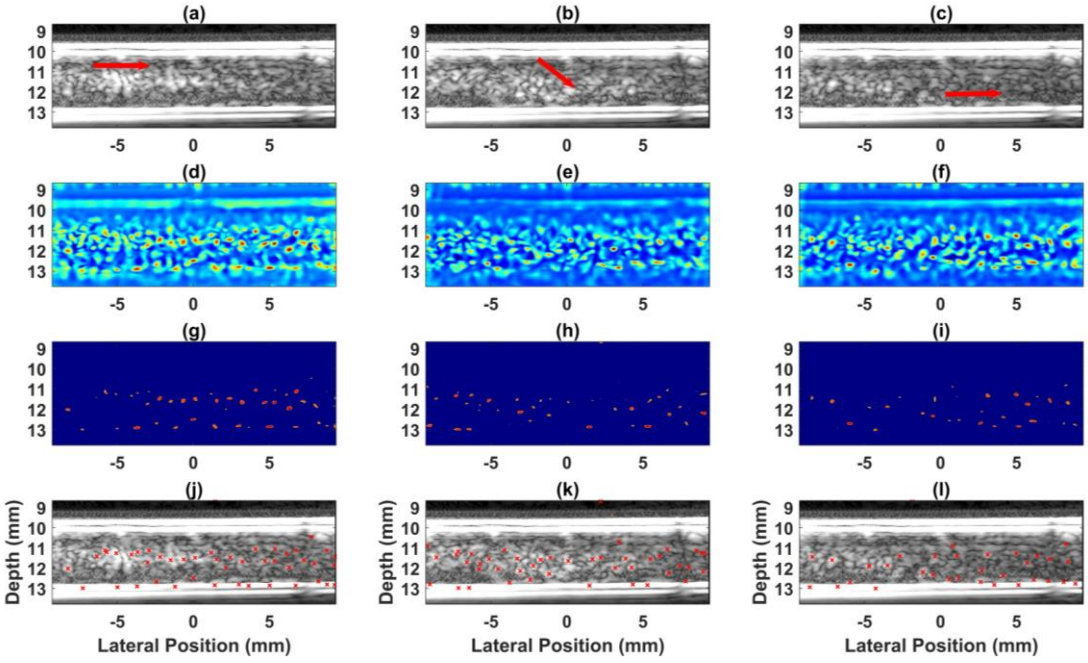

Figure 5.13. MB localization steps under ARF for 1300, 1700 and 2800 frame numbers respectively (a), (b), (c) represent the B-mode images (d), (e), (f) represent images after 2D-CC with PSF (g, (h), (i) represent images after threshold (j), (k), (l) represent the detected center of MBs.

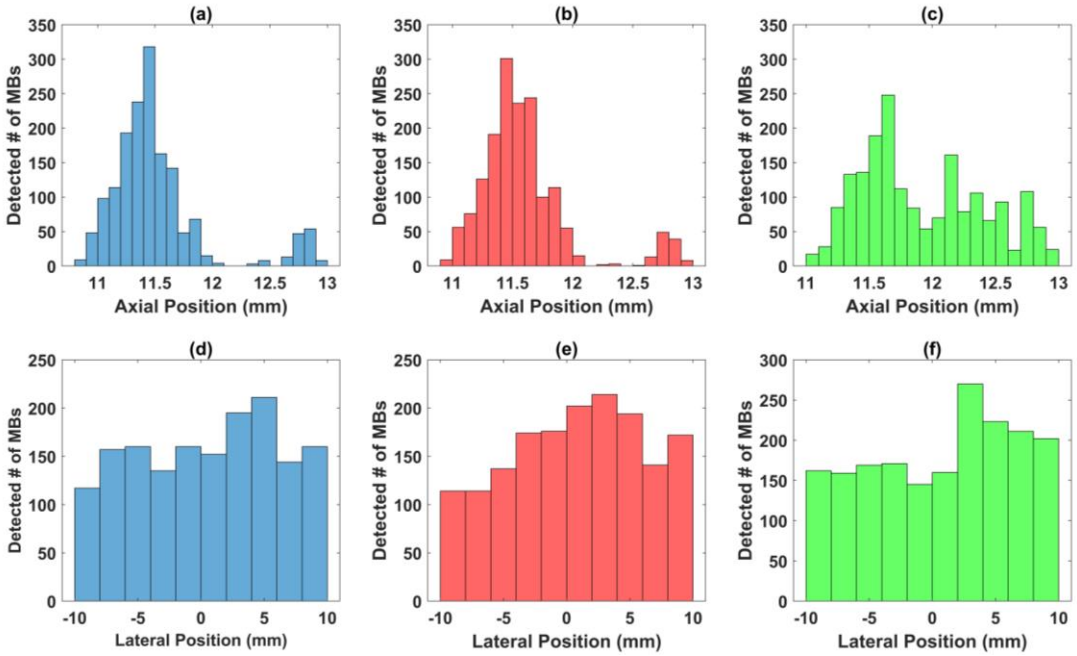

Figure 5.14. Histogram of detected MBs in (a), (b), (c) axial position for frames 800-1300, 1500-2000 and 2500-3000 respectively. (d), (e), (f) lateral position for frames 800-1300, 1500-2000 and 2500-3000 respectively.

It can be concluded from Figure 5.14 and Figure 5.13 that MB population is the highest at x= -5, z=11.5 mm in the first frames. However, the detected number of MBs are significantly increased in the last received frames at x=12.5 mm which proves that MBs are pushed through the bottom of the capillary tube with ARF transmits.

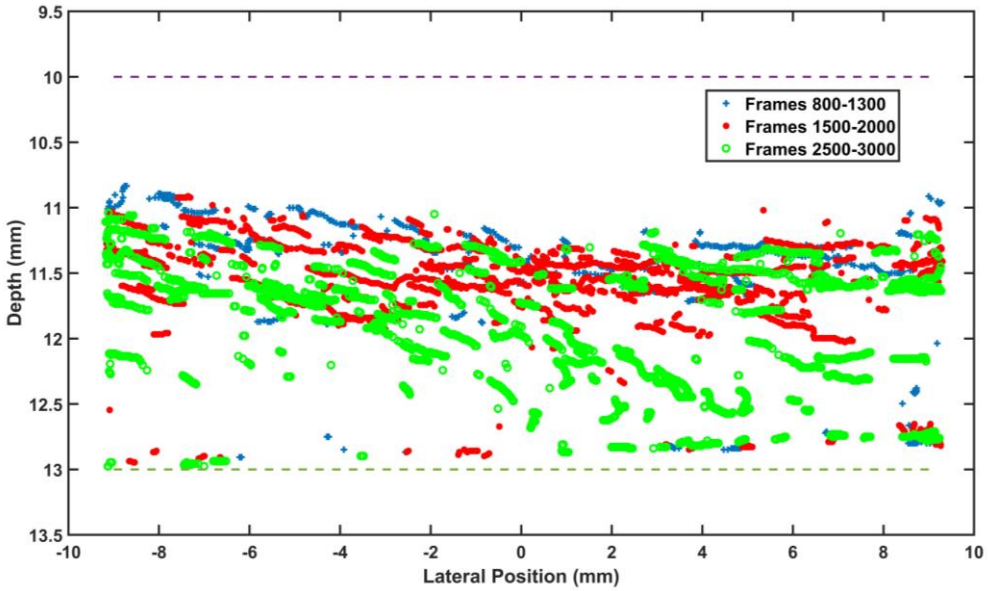

Figure 5.15. MB localizations with 30 frames obtained from frames 800-1300, 1500-2000 and 2500-3000 respectively.

5.3 Quality Metrics

Contrast-to-noise ratio (CNR) and contrast-to-tissue ratio (CTR) were calculated in order to quantitatively evaluate the proposed imaging methods. During experiments, transducer was positioned perpendicular to capillary tubes so that MB-filled tube, water-filled tube and tissue regions can be imaged at the same time. Three region of interests (ROIs) are manually positioned in saved images. ROI sizes are set to 50x50 pixels and hence area of 2500 pixels. ROIs were selected for tissue, MBs, water regions and colored green, red, blue respectively as shown in Figure 5.16. CTR and CNR of the images are calculated by Equations 5.1 and 5.2.

$$\mathrm{CNR} = 20\log_{10}\left(\frac{|\mu_{MB}-\mu_{water}|}{\sqrt{{\sigma_{MB}}^2+{\sigma_{water}}^2}}\right) \tag{5.1}$$

$$\mathrm{CTR} = 20\log_{10}\left(\frac{|\mu_{MB}-\mu_{tissue}|}{\sqrt{{\sigma_{MB}}^2+{\sigma_{tissue}}^2}}\right) \tag{5.2}$$

where μ_{MB}, μ_{tissue}, μ_{water} represent mean pixel value and σ_{MB}, σ_{tissue}, σ_{water} represent standard deviation of the MB, tissue and water regions respectively.

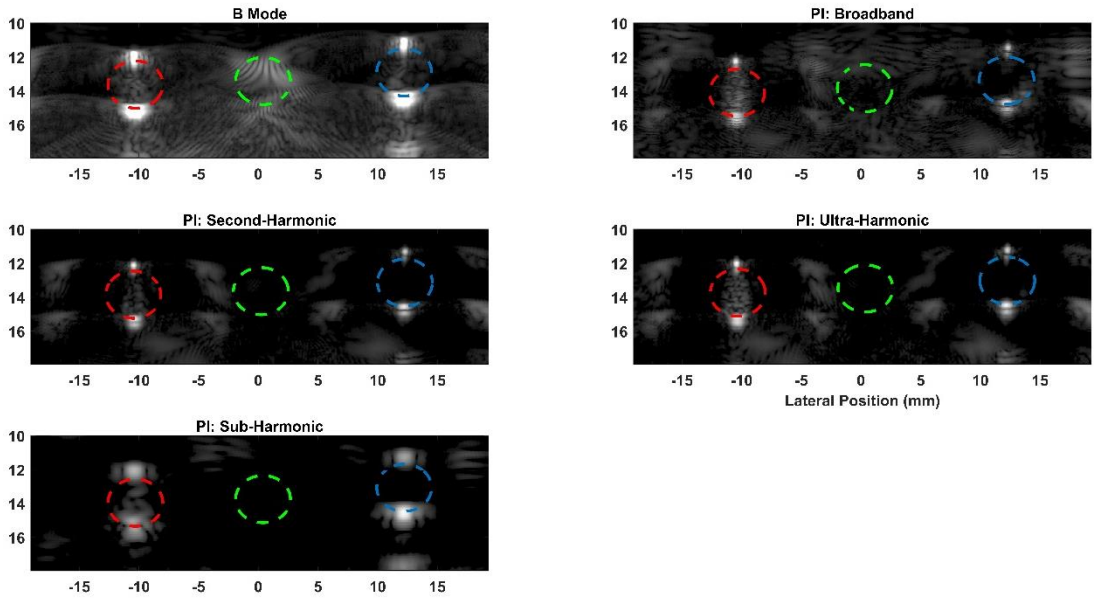

Figure 5.16. ROI selection for MB (red dashed line), tissue (green dashed line), water (blue dashed line).

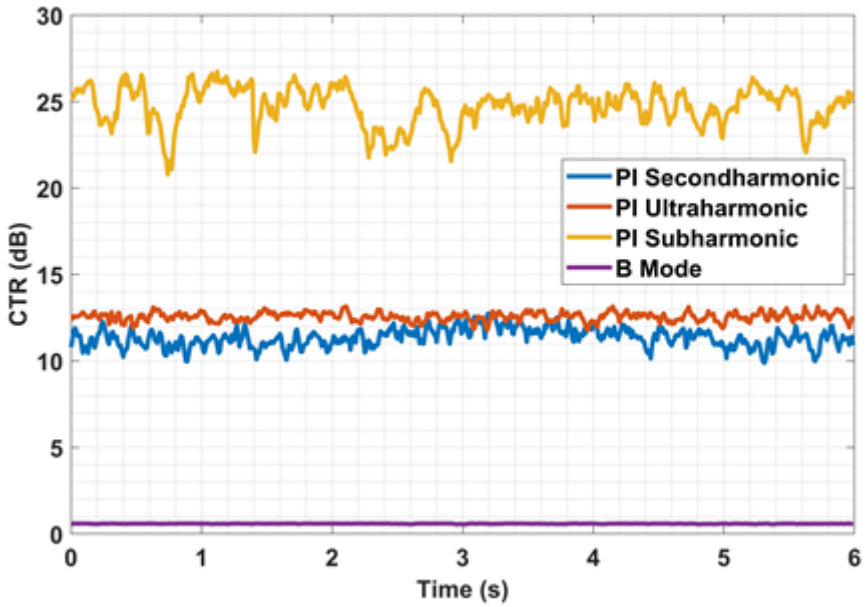

Figure 5.17. CTR calculations for PI applied in second harmonic, subharmonic and ultraharmonic regions and B mode.

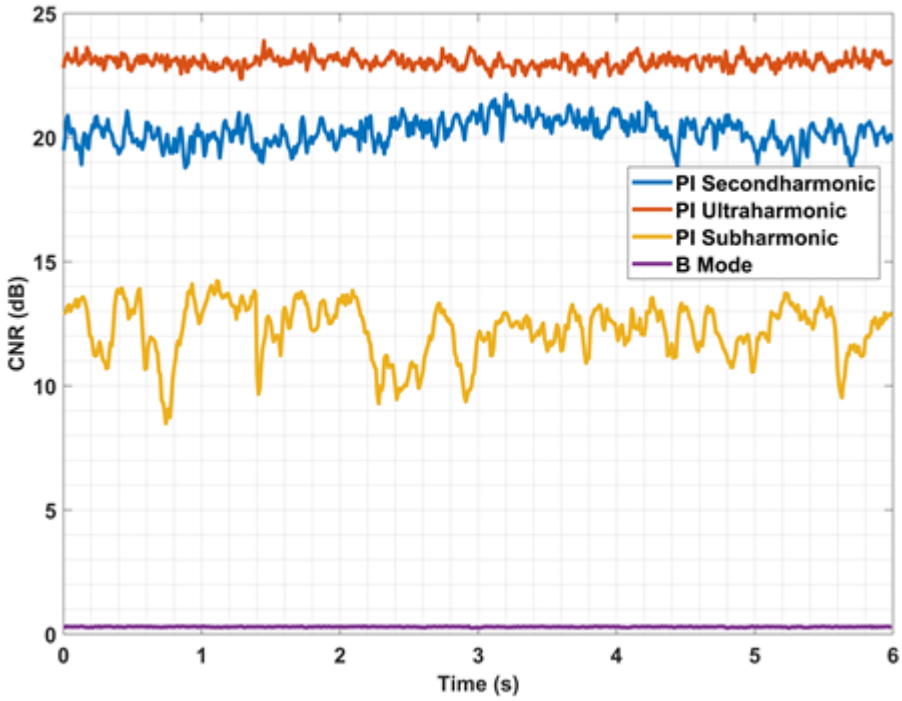

Figure 5.18. CNR calculations for PI applied in second harmonic, subharmonic and ultraharmonic regions and B mode.

Figure 5.17 and Figure 5.18 are showing the CTR and CNR values calculated for each frame of the acquired images. The averaged CTR and CNR results for imaging techniques are summarized in Table 5.1. PI improved contrast more than 10 dB compared to B-mode. Among the harmonic regions of PI applied experiments, subharmonic region has showed the best CTR whereas ultraharmonic region has showed the best CNR value.

Table 5.1. Imaging Techniques Evaluation in terms of CTR and CNR

Techniques	CTR (dB)	CNR (dB)
B-Mode	1	1
Second-harmonic PI	11	20
Ultraharmonic PI	12	23
Subharmonic PI	25	12

CHAPTER 6

CONCLUSION

An ultrasound imaging method combining acoustic radiation force (ARF) and ultrafast ultrasound imaging technique is developed in this thesis. This new technique is capable of very fast and reliable detection of specific disease cells by introducing tagged-microbubbles into the blood flow and directing these tagged-MBs with ARF to increase cell-MB interaction and simultaneously image the area. Plane waves with coherent compounding angles were used for ultrafast imaging. To demonstrate this new technique, a setup was created with homemade tissue mimicking phantom formed by agar, the Verasonics Vantage Research System the 128-elements L11-5v linear array transducer in order to implement ultrasound imaging techniques, the syringe pump and phosphate buffered saline (PBS) with SIMB4-5/SIMB5-8 suspension for imitating blood flow. Then, microbubbles are localized by applying ultrasound localization microscopy (ULM) methods, which increases spatial resolution of ultrasound images and makes individual detection of MBs possible although MBs are smaller than diffraction limit.

Only coherent compounding plane wave imaging was initially used for the post-processing algorithm development. The most challenging imaging condition was the dense MBs flowing with lower speeds since resolution extracted by PSF would not be good enough to differentiate individual MBs standing close to each other. In this condition, SVD & DI methods clean up the slowly moving and stationary MBs and therefore localization fails. On the other hand, PI method is the less sensitive method to flow speed. However, PI method is highly dependent on bandwidth of the transducer and it restricts the center frequency selection. PI experiments are conducted by second order, ultraharmonic and subharmonic filtering in order to remove artifacts and CNR, CTR values were calculated in comparison with B-mode

imaging. MB detections obtained by DI and SVD are compared and DI is found to be less accurate due to its inability to remove tissue signals completely.

FUS transmits were added into coherent compounding plane wave imaging sequence in order to take advantage of the ARF created by the focused transmits. The flow speed and the push performance of ARF added ultrafast imaging is closely related. In lower flow speeds, ARF dominates and MBs were pushed through the bottom whereas in high flow speeds, drag force of the flow dominates and MBs can be pushed only shallower depths when the same settings of transmit pulses are used. In addition, the effect of usage frequency of FUS transmits were investigated such that FUS transmits were inserted in between compounding angle transmits of each image frame and FUS transmits are inserted only in between each imaging frames. It was expected to obtain stronger push effect for the former method since frequency of FUS application is increased. However, such effect could not be observed. By using the latter method for ARF introduction to the sequence, MBs were observed to move downward direction successfully.

In summary, ULM method was successfully implemented and MBs were detected by using coherent compounding plane wave imaging. Our study shows that ultrafast ultrasound imaging with ARF has a great potential for molecular imaging due to the push effect emerged by the ARF without disrupting imaging sequence and lowering the frame rate. As a future work, developed imaging method can be applied by using streptavidin coated MBs in an antibody covered capillary tube in order to test its effectiveness in terms of MB-antibody interaction.

REFERENCES

[1] R.S. Moorthy, “Doopler Ultrasound,” Med J Armed Forces India, vol. 58, no. 1, pp. 1-2, Jan. 20002.

[2] R. M. Sigrist, J. Liau, A. E. Kaffas, M. C. Chammas, and J. K. Willmann, “Ultrasound elastography: Review of techniques and clinical applications,” Theranostics, vol. 7, no. 5, pp. 1303–1329, 2017.

[3] P. Santos, A.M. Petrescu, J. Pedrosa, M. Orlowska, V. Komini, J.U. Voigt and J. D’hooge, "Natural Shear Wave Imaging in the Human Heart: Normal Values, Feasibility, and Reproducibility," in IEEE Transactions on Ultrasonics, Ferroelectrics, and Frequency Control, vol. 66, no. 3, pp. 442-452, March 2019.

[4] M. Tanter and M. Fink, “Ultrafast imaging in biomedical ultrasound” in IEEE Transactions on Ultrasonics, Ferroelectrics, and Frequency Control, vol. 61, no. 1, pp. 102-119, January 2014.

[5] J. Brown, K. Christensen-Jeffries, S. Harput, C. Dunsby, M. X. Tang, and R. J. Eckersley, “Investigation of microbubble detection methods for super-resolution imaging of microvasculature,” in Proc. IEEE Int. Ultrason. Symp. (IUS). pp. 1–4, Sep. 2017.

[6] K. Christensen-Jeffries, O. Couture, P.A. Dayton, Y.C. Eldar, K. Hynynen, F. Kiessling, M. O'Reilly, G.F. Pinton, G. Schmitz, M.X Tang, M. Tanter, and van R. Sloun, “Super-resolution Ultrasound Imaging,” Ultrasound in medicine and biology, vol. 46, no. 4, pp. 865–891, 2020.

[7] X. Qian, H. Kang, R. Li, G. Lu, Z. Du, K.K Shung, and Q. Zhou, “In Vivo Visualization of Eye Vasculature Using Super-Resolution Ultrasound Microvessel Imaging,” in IEEE Transactions on Biomedical Engineering, vol. 67, no. 10, pp. 2870-2880, Oct. 2020.

[8] D. Buonsenso, A. Piano, F. Raffaelli, N. Bonadia, K. de Gaetano Donati, and F. Franceschi, “Point-of-Care Lung Ultrasound findings in novel coronavirus disease-

19 pnemoniae: a case report and potential applications during COVID-19 outbreak," European review for medical and pharmacological sciences, vol. 24, no. 5, pp. 2776–2780, 2020.

[9] P.Y. Chen, T.H. Yang, L.C. Kuo, C. C. Shih and C. C. Huang, "Characterization of Hand Tendons Through High-Frequency Ultrasound Elastography," in IEEE Transactions on Ultrasonics, Ferroelectrics, and Frequency Control, vol. 67, no. 1, pp. 37-48, Jan. 2020.

[10] S.P. Arjunan, M.C. Thomas, "A Review of Ultrasound Imaging Techniques for the Detection of Down Syndrome," IRBM, vol. 41, no. 2, pp. 115-123, 2020.

[11] A. Nabavizadeh, T. Payen, A.C Iuga, I.R Sagalovskiy, D. Desrouilleres, N. Saharkhiz, C.F. Palermo, S.A. Sastra, P.E. Oberstein, V. Rosario, M.D. Kluger, B.A. Schrope, J.A. Chabot, K.P. Olive, and E.E. Konofagou, "Noninvasive Young's modulus visualization of fibrosis progression and delineation of pancreatic ductal adenocarcinoma (PDAC) tumors using Harmonic Motion Elastography (HME) in vivo," Theranostics, vol. 10, no. 10, pp. 4614–4626, 2020.

[12] C. Rabut, M. Correia, V. Finel, S. Pezet, M. Pernot, T. Deffieux, and M. Tanter, "4D functional ultrasound imaging of whole-brain activity in rodents," Nature methods, vol. 16, no. 10, pp. 994–997, 2019.

[13] A. Novell, H.A.S. Kamimura, A. Cafarelli, M. Gerstenmayer, J. Flament, J. Valette, P. Agou, A. Conti, E. Selingue, R. Aron Badin, P. Hantraye, and B. Larrat, "A new safety index based on intrapulse monitoring of ultraharmonic cavitation during ultrasound-induced blood-brain barrier opening procedures," Sci Rep, vol. 10, pp. 10088, 2020.

[14] Y. Tian, Z. Liu, H. Tan, J. Hou, X. Wen, F. Yang, and W. Cheng, " New Aspects of Ultrasound-Mediated Targeted Delivery and Therapy for Cancer," International journal of nanomedicine, vol. 15, pp. 401–418, 2020.

[15] B.T. Khuri-Yakub, and O. Oralkan, "Capacitive micromachined ultrasonic transducers for medical imaging and therapy", Journal of micromechanics and

microengineering: structures, devices, and systems, vol. 21, no. 5, pp. 54004-54014, 2011.

[16] O. Villemain, J. Baranger, M.K. Friedberg, C. Papadacci, A. Dizeux, E. Messas, M. Tanter, MM. Pernot, and L. Mertens, “Ultrafast Ultrasound Imaging in Pediatric and Adult Cardiology: Techniques, Applications, and Perspectives,” JACC. Cardiovascular imaging, vol. 13, no. 8, pp. 1771–1791, 2020.

[17] G. Montaldo, M. Tanter, J. Bercoff, N. Benech and M. Fink, "Coherent plane-wave compounding for very high frame rate ultrasonography and transient elastography," in IEEE Transactions on Ultrasonics, Ferroelectrics, and Frequency Control, vol. 56, no. 3, pp. 489-506, March 2009.

[18] O. Couture, M. Fink and M. Tanter, "Ultrasound contrast plane wave imaging," in IEEE Transactions on Ultrasonics, Ferroelectrics, and Frequency Control, vol. 59, no. 12, pp. 2676-2683, Dec. 2012.

[19] A. Ng and J. Swanevelder., “Resolution in ultrasound imaging,” Continuing Education in Anaesthesia Critical Care Pain, vol. 11, no. 5, pp. 186–192, 2011.

[20] Y. Desailly, J. Pierre, O. Couture, and M. Tanter, “Resolution limits of ultrafast ultrasound localization microscopy,” Phys. Med. Biol., vol. 60, no. 22, pp. 8723–8740, Nov. 2015.

[21] O.M. Viessmann, R.J. Eckersley, K. Christensen-Jeffries, M.X. Tang, and C. Dunsby, “Acoustic super-resolution with ultrasound and microbubbles,” Physics in medicine and biology, vol. 58, no. 18, pp. 6447–6458, 2013.

[22] C. Errico, J. Pierre, S. Pezet, Y. Desailly, Z. Lenkei, O. Couture, and M. Tanter, “Ultrafast ultrasound localization microscopy for deep super-resolution vascular imaging,” Nature, vol. 527, pp. 499–502, Nov. 2015.

[23] F. Lin, S.E. Shelton, D. Espíndola, J.D. Rojas, G. Pinton, and P.A. Dayton, “3-D Ultrasound Localization Microscopy for Identifying Microvascular Morphology

Features of Tumor Angiogenesis at a Resolution Beyond the Diffraction Limit of Conventional Ultrasound", Theranostics, vol. 7, no. 1, pp. 196–204, 2017.

[24] T. A. Whittingham, "Contrast Specific Imaging Techniques: Technical Point of View", Contrast Media in Ultrasonography Basic Principles and Clinical Applications, 2005.

[25] Y. Desailly, O. Couture, M. Fink, and M. Tanter, "Sono-activated ultrasound localization microscopy," Appl. Phys. Lett., vol. 103, no. 17, p. 174107, 2013.

[26] P. Song, J.D. Trzasko, A. Manduca, R. Huang, R. Kadirvel, D.F. Kallmes, and S. Chen "Improved Super-Resolution Ultrasound Microvessel Imaging With Spatiotemporal Nonlocal Means Filtering and Bipartite Graph-Based Microbubble Tracking," in IEEE Transactions on Ultrasonics, Ferroelectrics, and Frequency Control, vol. 65, no. 2, pp. 149-167, Feb. 2018.

[27] C. Shen, Y. Chou, P.C. Li, "Pulse Inversion Techniques in Ultrasonic Nonlinear Imaging", Journal of Medical Ultrasound, vol. 13, no. 1, pp. 3-17, 2005.

[28] C. Tremblay-Darveau, R. Williams, L. Milot, M. Bruce and P. N. Burns, "Combined perfusion and doppler imaging using plane-wave nonlinear detection and microbubble contrast agents," in IEEE Transactions on Ultrasonics, Ferroelectrics, and Frequency Control, vol. 61, no. 12, pp. 1988-2000, Dec. 2014,

[29] C. Kollmann, "New sonographic techniques for harmonic imaging--underlying physical principles," European journal of radiology, vol. 64, no. 2, pp. 164–172, 2005.

[30] R. Basude, M.A. and Wheatley, "Generation of ultraharmonics in surfactant-based ultrasound contrast agents: use and advantages". Ultrasonics, vol. 39, no. 6, pp. 437–444, 2001.

[31] A. Anvari, F. Forsberg, A.E. and Samir, "A Primer on the Physical Principles of Tissue Harmonic Imaging" Radiographics, vol. 35, no. 7, pp. 1955–1964, 2015.

[32] W. R. Hedrick, L. Metzger, “Tissue Harmonic Imaging: A Review.”, Journal of Diagnostic Medical Sonography, vol. 21, no. 3, pp.183–189, 2005.

[33] M.A. Averkiou, M.F. Bruce, J.E. Powers, P.S. Sheeran, and P.N. Burns, “Imaging Methods for Ultrasound Contrast Agents,” Ultrasound in medicine and biology, vol. 46, no. 3, pp. 498–517, 2020.

[34] A. Eller and H. G. Flynn, "Generation of Subharmonics of Order One-Half by Bubbles in a Sound Field", The Journal of the Acoustical Society of America, vol. 46, 722-727, 1969.

[35] W. Lauterborn, "Numerical investigation of nonlinear oscillations of gas bubbles in liquids", The Journal of the Acoustical Society of America, vol. 59, pp. 283-293, 1976.

[36] A. Katiyar and K. Sarkar, “Excitation threshold for subharmonic generation from contrast microbubbles”, The Journal of the Acoustical Society of America, vol. 130, no. 5, pp. 3137–3147, 2011.

[37] H. Shekhar, I. Awuor, K. Thomas, J.J. Rychak and M.M. Doyley, “The delayed onset of subharmonic and ultraharmonic emissions from a phospholipid-shelled microbubble contrast agent”, Ultrasound in medicine & biology, vol. 40, no. 4, pp. 727–738, 2014.

[38] Y. Jiao, D. Zhang, Y. Xu, Y Chen, Z Wu, and Y. Cui, “ H-scan Subtraction Doppler Imaging: A Novel Ultrasound Small Blood Vessel Flow Characterization with Scattering and Reflection Identification,” Applied Sciences, vol. 10, no. 21, pp. 7604, 2020.

[39] A. Mehrem, “Theoretical study of microbubble dynamics under the action of ultrasound fields”, M.S – Master of Science, Universitat Politècnica de València. 2013.

[40] I.G. Newsome, T.M. Kierski, and P.A. Dayton, “Assessment of the Superharmonic Response of Microbubble Contrast Agents for Acoustic

Angiography as a Function of Microbubble Parameters," Ultrasound in medicine and biology, vol. 45, no. 9, pp. 2515–2524, 2019.

[41] Bracco, "Technical sheet of Lumason", Bracco Imaging, 2021.

[42] A. Dauba, A. Delalande, H. Kamimura, A. Conti, B. LarratN. Tsapis, and A. Novell "Recent Advances on Ultrasound Contrast Agents for Blood-Brain Barrier Opening with Focused Ultrasound," Pharmaceutics, vol. 12, no. 11, pp. 1125, 2020.

[43] M. Kaya, S. Feingoldi, K. Hettiarachchi, A.P. Lee, and P.A. Dayton, "Acoustic responses of monodisperse lipid-encapsulated microbubble contrast agents produced by flow focusing," Bubble science engineering and technology, vol. 2, no. 2, pp. 33-40, 2010.

[44] R. Daigle, "Vantage Sequence Programming Tutorial" Verasonics, Inc., July, 2017.

[45] Verasonics, Inc., "Vantage Sequence Programming Manual",November, 2019.

[46] S. Harput, L. Nie, D.M.J. Cowell, T. Carpenter, B. Raiton, J. McLaughlan, S. Freear, "Simultaneous Acoustic Trapping and Imaging of Microbubbles at Clinically Relevant Flow Rates" Pyhsics.Med-ph, Feb. 2019.

[47] T. Furnival, R. K. Leary, and P. A. Midgley, "Denoising time-resolved microscopy image sequences with singular value thresholding," Ultramicroscopy, vol. 178, pp. 112–124, Jul. 2017.

[48] C. Demené, T. Deffieux, M. Pernot, B.F. Osmanski, V. Biran, J.L. Gennisson, L.A. Sieu, A. Bergel, S. Franqui, J.M. Correas, I. Cohen, O. Baud, and M. Tanter "Spatiotemporal Clutter Filtering of Ultrafast Ultrasound Data Highly Increases Doppler and fUltrasound Sensitivity," in IEEE Transactions on Medical Imaging, vol. 34, no. 11, pp. 2271-2285, Nov. 2015,

[49] J. Kim, Q. Wang, S. Zhang, and S. Yoon, "Compressed Sensing-Based Super-Resolution Ultrasound Imaging for Faster Acquisition and High Quality

Images," IEEE transactions on bio-medical engineering, vol. 68, no. 11, pp. 3317–3326, 2021.

[50] P. Song, A. Manduca, J.D. Trzasko, and S. Chen, "Ultrasound Small Vessel Imaging with Block-Wise Adaptive Local Clutter Filtering," in IEEE Transactions on Medical Imaging, vol. 36, no. 1, pp. 251-262, 2017.

[51] G. Pinton, G. Trahey and J. Dahl, "Spatial coherence in human tissue: implications for imaging and measurement.", IEEE transactions on Ultrasonics, Ferroelectrics, and Frequency Control, vol. 61, no. 12, pp. 1976–1987, 2014.

[52] M. A. Lediju, , G. E. Trahey, B.C. Byram and J. J. Dahl, "Short-lag spatial coherence of backscattered echoes: imaging characteristics.", IEEE transactions on Ultrasonics, Ferroelectrics, and Frequency Control, vol. 58, no. 7, pp. 1377–1388, 2011.

[53] E. Hecht, "Temporal Resolution: Optics", United States of America: Addison Wesley, vol. 4, 2002.

[54] Y. Jiao, D. Zhang, Y. Xu, Y. Chen, Z. Wu, and Y. Cui, "H-scan Subtraction Doppler Imaging: A Novel Ultrasound Small Blood Vessel Flow Characterization with Scattering and Reflection Identification," Applied Sciences, vol. 10, no. 21, pp. 7604, 2020.

[55] R. Muthaiah, K. NeelaKantan, V. Sharma, and A. Arora, "Image Compression and Reconstruction using Cubic Spline Interpolation Technique," American Journal of Applied Sciences, vol. 5, no. 11, pp. 1562-1565, 2008.

[56] Simpletracker. MathWorks. (n.d.). Retrieved January 15, 2022, from https://www.mathworks.com/matlabcentral/fileexchange/34040-simpletracker

[57] F. Foroozan, M.A. O'Reilly and & K. Hynynen, "Microbubble Localization for Three-Dimensional Superresolution Ultrasound Imaging Using Curve Fitting and Deconvolution Methods.", IEEE transactions on bio-medical engineering, vol. 65, no. 12, pp. 2692–2703, 2018.